High-resolution OSL dating of loess in Adventdalen, Svalbard: Late Holocene dust activity and permafrost development

Christian F. Rasmussen [a, b], Hanne H. Christiansen [b], Jan-Pieter Buylaert [c], Alastair Cunningham [c], Ramona Schneider [d], Mads F. Knudsen [a], Thomas Stevens [d, e, *]

[a] Department of Geoscience, Aarhus University, Høegh-Guldbergs Gade 2, 8000, Aarhus, Denmark
[b] Department of Arctic Geophysics, University Centre in Svalbard, Longyearbyen, 9170, Svalbard, Norway
[c] Department of Physics, Technical University of Denmark, Frederiksborgvej 399, 4000, Roskilde, Denmark
[d] Department of Earth Sciences, Uppsala University, Villavägen 16, 75236, Uppsala, Sweden
[e] Department of Geosciences and Geography, University of Helsinki, P.O. Box 64, 00014, Helsinki, Finland

ARTICLE INFO

ABSTRACT

There is considerable uncertainty over the nature and causes of Holocene dust activity in the Arctic, and its links to climatic changes. Loess deposits act as near-source archives of dust deposition and provide a means to address these uncertainties. Here we develop a fully independent age model for a loess core taken in Adventdalen, Svalbard, based on 136 quartz luminescence ages taken at 2 cm intervals. This represents the most detailed luminescence dating analysis undertaken to date on a sedimentary archive. Extensive laboratory tests and stratigraphic consistency indicate that the quartz luminescence ages are reliable. Together with grain size and cryostratigraphic analyses, as well as stratigraphic investigation of an adjacent loess exposure, the exceptional detail of the chronology combined with Bayesian age modelling uniquely allows changes in loess accumulation rates, particle size and permafrost development to be reconstructed over the last 3000 yrs on 10^1–10^3 yr timescales. The results show that loess deposition was mostly continuous over this interval, albeit with a short period of reworking or non-aeolian sedimentation during the Little Ice Age. Permafrost development in the loess is dominantly syngenetic, with ice contents increasing with depth. There is considerable variability in loess mass accumulation rate over the late Holocene, with peaks occurring during the last 250 yrs, as well as at 750–900, 1050–1200, 1400–1600, 1900–2450 and possibly 2700–3000 a. These peaks generally coincide with increased coarse silt deposition, potentially suggesting a link with greater wind activity. However, the peaks also seem to coincide with possible warm phases on Svalbard, which would rather imply that temperature-driven sediment availability in glaciofluvial source areas is the main control on dustiness in Adventdalen. In any case, the rates of loess deposition in the Adventdalen core are exceptionally high globally (up to 0.35 cm yr^{-1}/2900 g m^{-2} yr^{-1} sedimentation and mass accumulation rates, respectively), and if representative of wider patterns across Svalbard, may suggest that the archipelago is a more important high latitude dust source than previously realised.

1. Introduction

High latitude atmospheric mineral dust (dominantly clay and silt-sized particles at >50° N; Bullard et al., 2016; Meinander et al., 2022) is increasingly recognised as a critical yet poorly understood component of the climate system (Bullard et al., 2016). Recent evidence suggests that modern dust in Arctic regions is dominantly sourced in the high latitudes, raising questions over the extent to which this dust affects Arctic to global climate change, and over how high latitude dust impacts the complex mechanisms behind Arctic amplification. Despite this importance, high latitude dust sources and dust emission variability are still poorly understood, especially in the past. Indeed, synthesis of well-constrained Holocene dust deposition records (Albani et al., 2015) reveals a conspicuous lack of data from the Arctic Eurasia, with only a few isolated records available from other northern high latitudes. This

* Corresponding author. Department of Earth Sciences, Uppsala University, Villavägen 16, 75236, Uppsala, Sweden.
E-mail address: thomas.stevens@geo.uu.se (T. Stevens).

gap means that the specific causes of past changes in dust emission from the Arctic are unclear, greatly limiting our understanding of how dust and climate in the region interact. Given the sensitivity of the Arctic to climate change, and the role of Arctic climate feedbacks in driving global climate change (Overland et al., 2019), it is critical that well-dated records of past dust and climate change from the Arctic are developed.

Arctic loess deposits are a potential means to address this need. Loess deposits comprise wind-blown dust accumulated on land, and are widely used as past climate archives (Schaetzl et al., 2018). Loess is also an excellent archive of near source 'coarse' dust (>5 μm), the past activity of which is particularly poorly understood. Coarse dust particles also have specific climatic significance, including disproportionately acting as ice nuclei and driving net radiative warming, in contrast to the net cooling induced through fine dust (Adebiyi and Kok, 2020). Loess is widespread in the mid-latitudes, but more spatially restricted deposits of loess are also found in multiple parts of the northern high latitudes, including Alaska (Muhs et al., 2003), eastern Canada (Fortier et al., 2006), Greenland (Willemse et al., 2003), Iceland (Jackson et al., 2005), Sweden (Stevens et al., 2022), Svalbard (Bryant, 1982) and Siberia (Volvakh et al., 2022). These deposits represent an important opportunity to investigate coupled past climate and dust variability in high latitude environments. Furthermore, high latitude loess formation often occurs in periglacial environments that likely experience permafrost formation (Zech et al., 2008; Gilbert et al., 2018), the development of which affects global carbon cycling and high latitude landscape processes.

In order to fully utilise loess records to understand past dust deposition it is critical that detailed independent age models from loess are coupled to climate proxy and stratigraphic analyses (Perić et al., 2022). Currently, however, few studies of high latitude loess have employed detailed independent dating, especially in the High Arctic. Some luminescence and radiocarbon ages have been obtained on relatively thick loess (up to 3 m) deposited along terraces of the lower Advent River, in the Adventdalen valley, Svalbard, as part of wider studies of valley and permafrost evolution (Oliva et al., 2014; Cable et al., 2018; Gilbert et al., 2018). However, no detailed independent dating or past climate and dust analysis has been conducted on these loess deposits. Svalbard is known to have experienced major changes in past climate and is currently experiencing rates of climate change far greater than the global average (Nordli et al., 2020). Given their thickness, Adventdalen loess deposits represent an excellent opportunity to investigate past dust and wind dynamics in the High Arctic, and its links to climate variability. However, the majority of past climate studies in the region focus on temperature and precipitation (e.g., Mangerud and Svendsen, 2018), whereas wind and aeolian dust activity remain poorly known. Furthermore, given its location in the continuous permafrost zone, analysis of Adventdalen loess allows reconstruction of permafrost history in relation to dust activity and loess formation.

Here, we attempt to reconstruct late Holocene aeolian activity and permafrost development using a combination of sediment stratigraphy and loess mapping, cryostratigraphy, particle size analysis, and very high sampling resolution luminescence dating (2 cm intervals) of loess formed in a permafrost environment in Adventdalen, Svalbard. Our study represents a uniquely detailed reconstruction of past high latitude loess and aeolian dust activity, and provides the most detailed independent chronology for high latitude late Holocene loess and dust activity yet available.

2. Study area

Adventdalen is a glacially sculpted u-shaped valley ~35 km long and ~4 km wide at its widest, and is a tributary valley to the larger Isfjorden fjord system in central Svalbard (Fig. 1A). The archipelago of Svalbard is classified as Arctic Tundra according to the Köppen-Geiger climate classification scheme (Kottek et al., 2006), with an average yearly temperature of −4 °C (Humlum et al., 2003). Mean annual precipitation in Adventdalen is 190−200 mm, with most of the precipitation falling as snow (Førland et al., 2011; Eckerstorfer and Christiansen, 2011). The area surrounding Adventdalen consists of flat-topped plateau mountains of sedimentary rock dominated by sandstone and shales (Major and Nagy, 1972). Wind direction in Adventdalen is dominantly easterly (Fig. 2), which is broadly parallel to the overall orientation of the whole valley (Fig. 1) (Christiansen et al., 2013). This easterly dominance is even more pronounced during autumn (Fig. 2B), with somewhat increased westerly winds during other times of year (Fig. 2A). Relatively high wind speeds in winter (Table 1) combined with the flat valley floor result in much of the snow in the valley being removed (Eckerstorfer and Christiansen, 2011). Monthly mean observations of wind, temperature, humidity, and temperature for 2022 in Adventdalen are shown in Table 1.

The valley is fluvially dominated by the Advent River, a glacially fed, seasonally active 1.5 km wide braided river system. Alluvial fans dominate the terrain in the lower valley (Fig. 1B) and the banks of the river are made up of 2−3 m high terraces consisting of loess (Bryant, 1982; Tolgensbakk et al., 2000; Gilbert et al., 2018), which is still actively being deposited in the valley (Fig. 1C). Adventdalen is underlain by approx. 100 m of permafrost, which thins towards the coast (Humlum et al., 2003). The permafrost is interpreted to be of similar age as the loess due to its syngenetic appearance in these types of sediments in the valley (Gilbert et al., 2018). The thickness of the active layer depends on the landforms, but has been increasing by 1 cm yr^{-1} for the past 20 yrs in loess sediments in Adventdalen (Strand et al., 2020). River terraces and alluvial fans demonstrate extensive periglacial activity, hosting periglacial landforms such as ice-wedge polygons, mud-boils, and pingos.

The study site CS-1 is located on a large flat vegetated surface (Fig. 1B) and is an active research site currently subject to various geological, climatological, and biological investigations, as well as active layer monitoring (Strand et al., 2020) and permafrost thermal observations (Christiansen et al., 2021). Previous research at the site includes several sedimentological and geochronological investigations that are relevant to this study (Bryant, 1982; Cable et al., 2018; Gilbert et al., 2018). The top c. 3 m of sediment has been interpreted as consisting of loess (Fig. 1D) and has previously been demonstrated as suitable for quartz optically stimulated luminescence (OSL) dating (Cable et al., 2018; Gilbert et al., 2018). In Adventdalen, dust forming the loess deposits is likely not transported very far as the Advent River acts as the local dust source area, while the adjacent river terraces act as loess depositional areas (Bryant, 1982).

3. Methods

We present several results from multiple analytical methods enabling reconstruction of late Holocene dust deposition as loess in Adventdalen, and discuss its possible environmental causes. Sediment and landform mapping was conducted to showcase the spatial extent of loess and association with key landforms in Adventdalen. Three cores were extracted from site CS-1 for detailed luminescence dating and analysis of variations in grain-size, cryostratigraphy, and moisture content. In addition, one stratigraphic section was logged and sampled for grain-size in an exposure c. 20 m away on the river terrace.
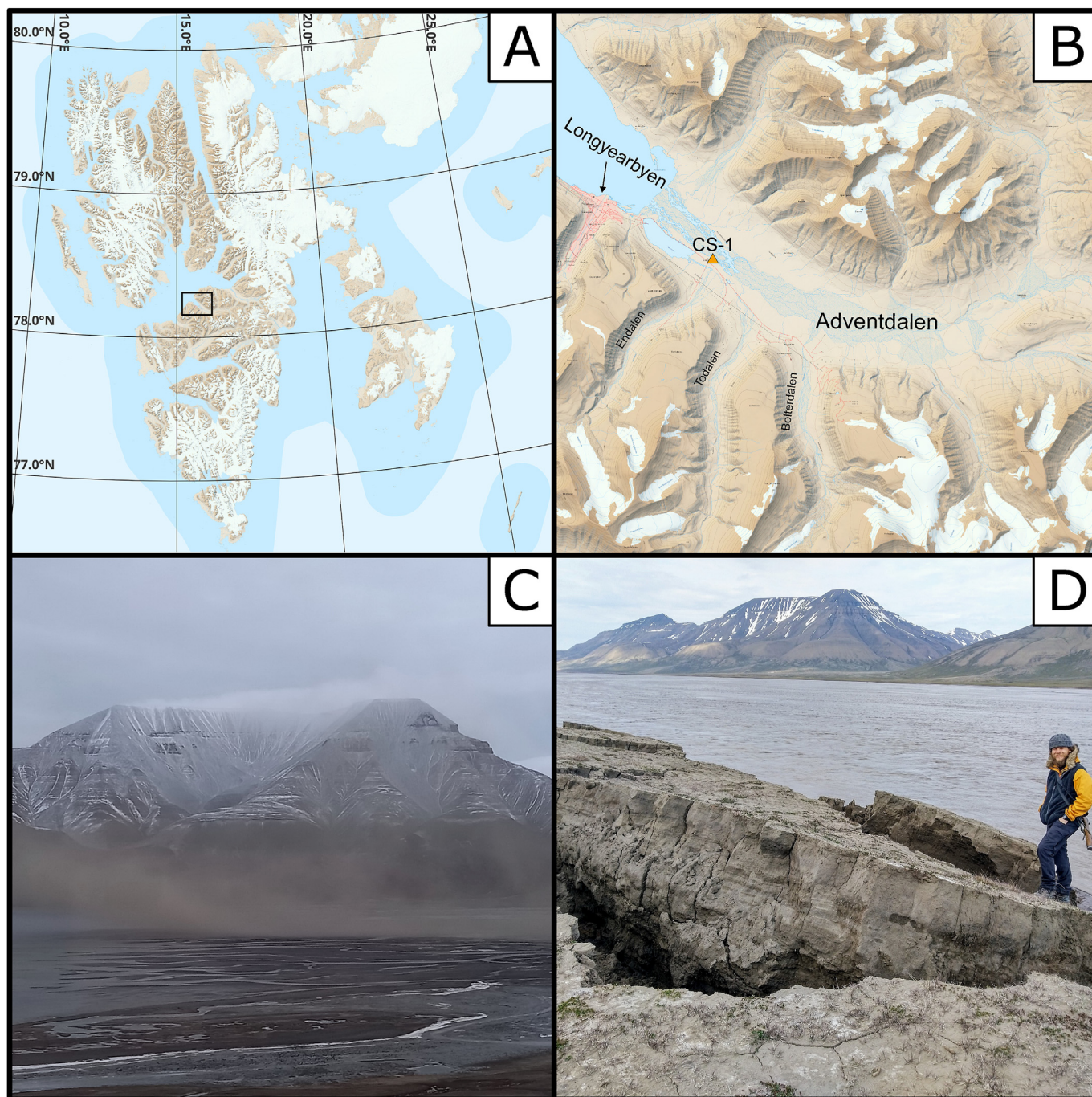
Fig. 1. A) Central Svalbard, with Adventdalen located in the black square. B) Location of study site CS-1 within Adventdalen (https://toposvalbard.npolar.no/). C) Dust storm in October 2020 in lower Adventdalen (photo Christiansen). D) Sediment exposed as a terrace section collapses into the Advent River (photo Rasmussen).

3.1. Loess mapping and modern aeolian regime in Adventdalen

A surface sediment and geomorphological map of Adventdalen, focusing on the spatial extent of loess, was produced by combining previous geomorphological mapping of Adventdalen including loess deposits (Tolgensbakk et al., 2000), previous field studies that identified loess in their study areas (Bryant, 1982; Jeppesen, 2001; Oliva et al., 2014; Gilbert et al., 2018), a study by Watanabe et al. (2017) that showed loess to be present on alluvial fans up to 700 m from the riverbank, and our field observations. Furthermore,

aerial photographs were utilized to determine whether alluvial fans are currently active. Loess deposition was assumed to affect non-active alluvial fans based on the findings of Watanabe et al. (2017). Modern wind direction and speed data shown in the Introduction (Fig. 2) are available from the weather station "Adventdalen" located close to the CS-1 site (78.203°N, 15.828 °E). Wind data are publicly available from the UNIS website (http://158. 39.149.183/Adventdalen/index.html#).
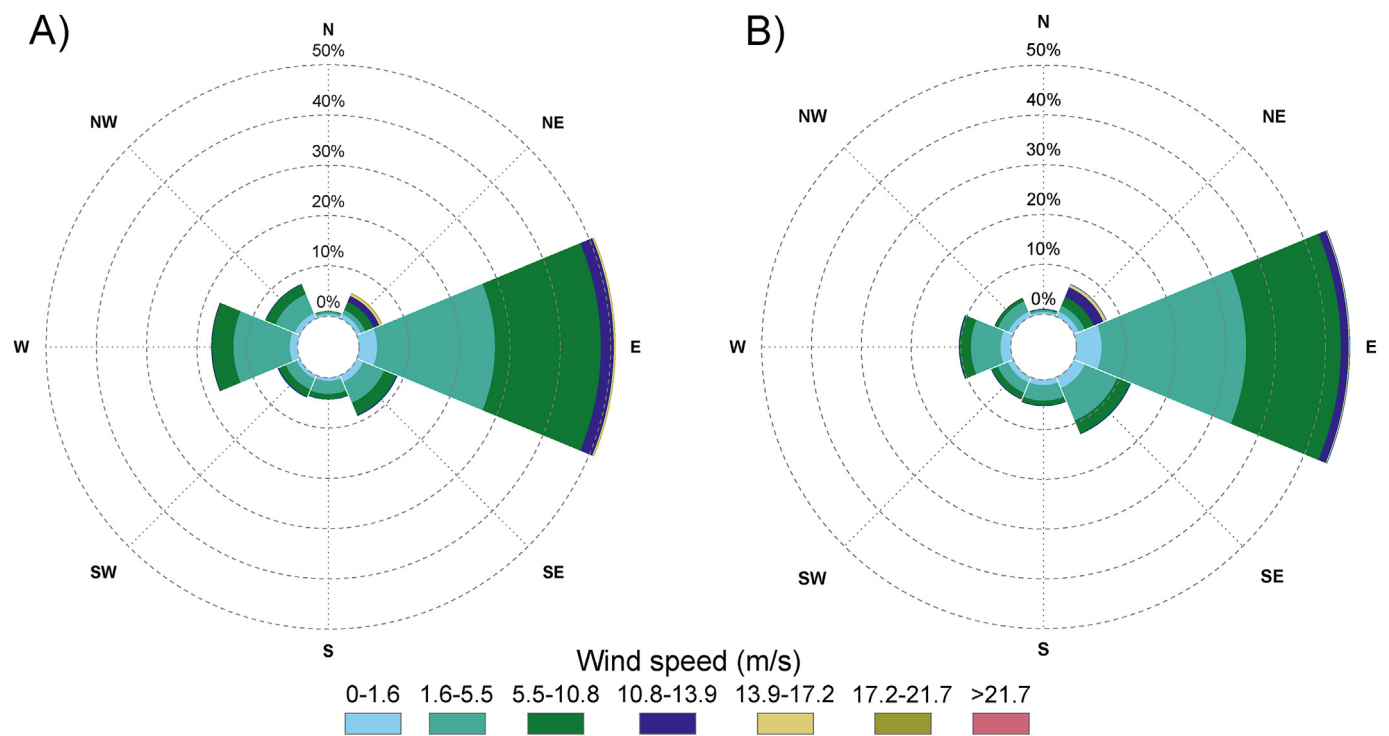
Fig. 2. Wind roses showing direction and windspeed groups from Adventdalen weather station (10 m height; near CS-1 site; 78.203 °N 15.828 °E). A: Average wind speed and direction 2016−2023. B: Average wind speed and direction September−November 2016−2023. Data available: https://www.unis.no/facilities/weather-stations/.

Table 1
2022 monthly data from Adventdalen weather station (78.203 °N 15.828 °E). Data from yr.no and https://www.unis.no/facilities/weather-stations/..

	Average wind speed (5 m) (m/s)	Average wind speed (10 m) (m/s)	Average temp (5 m) (°C)	Relative Humidity (%)	Precipitation (Total) (mm)
January	5.30	6.67	−11.86	78.89	NA
February	3.53	4.73	−14.89	80.86	NA
March	3.73	4.82	−9.36	79.98	32.8
April	4.43	5.60	−10.78	76.26	11.1
May	3.30	4.09	−2.25	79.00	3
June	5.49	6.63	5.64	80.87	13.5
July	4.36	5.43	8.93	83.70	4.5
August	3.43	4.37	6.52	84.26	36.6
September	3.49	4.53	2.89	86.95	26.3
October	3.24	4.34	−2.60	82.98	11.4
November	2.96	3.87	−1.38	85.78	21.6
December	3.52	4.52	−9.72	79.48	17.2

3.2. Sediment core extraction and exposed section sampling

The extraction of frozen sediment core samples was conducted over several days in September 2019 at the study site CS-1 (78.201°N, 15.840°E). An approximately 1.0 × 0.5 × 0.5 m soil pit was dug in the active layer and this unfrozen sediment was sampled with metal boxes (length: 23 cm, width: 15.6 cm, depth: 6 cm). Sampling of the underlying permafrozen sediment was conducted from the permafrost table, in the soil pit, by coring with a motorised hand drill model STIHL™ BT-121 Earth Auger. To extract the core, an unflighted open core barrel with square diamond cutting teeth was used. The core barrel has a diameter of 5 cm and the possibility to extract a core of a maximum length of 50 cm. At site CS-1, Gilbert et al. (2018) observed that the loess layer was 2.9 m thick, so coring was limited to the upper c. 3 m.

Three separate cores were extracted at site CS-1 and transported to frozen storage at the University Centre in Svalbard (UNIS) and kept at −5 °C. One of the cores (CS-1-A; 310 cm) was split

lengthwise setting aside one half for cryostratigraphy and the second half for grain-size measurements. The half intended for grain size measurements was divided into 4 cm sections and dried and packed for transport. Core CS-1-B (314.5 cm), which was used for OSL dating and gravimetric moisture/ice content, was divided into 140 individual 2 cm sections, and packed for transport, without drying. CS-1-C (322 cm) was put into frozen storage at UNIS.

A section at CS-1 was exposed in the terrace of the Advent River, c. 20 m NE of the coring site. After cleaning the exposure, stratigraphic and macro-sedimentary features were logged and photographs taken in August 2022. Samples for particle size were then taken continuously down the whole unfrozen part of the section at 5 cm intervals.

3.3. Cryostratigraphy

To understand and classify the development of permafrost, the cryostratigraphy of the CS-1 core was examined, including

description and interpretation based on the method of French and Shur (2010) as well as Gilbert et al. (2016). CS-1-A core sections were individually split on the long axis using a circular saw. All core sections were cleaned and analysed in the freeze laboratory at UNIS. The full core was exposed with a metre ruler to denote depth from the permafrost table, and the entire length was then photographed. The core pictures were digitally combined, and a cryostratigraphic description was conducted of the full-length core, identifying beginning-depth and end-depth of each cryostructure. The ground ice content was measured down the core in 2 cm intervals, and provided as gravimetric ice content and excess ice content, where this existed.

3.4. Grain-size analyses

Grain-size analysis is a powerful tool in assessing the nature of aeolian transport and potential reworking in loess sediments (Schaetzl and Attig, 2013; Újvári et al., 2016; Vandenberghe, 2013). Grain size analysis on core CS-1-A was conducted at the Department of Geoscience, University of Aarhus, using a Sympatec HELOS laser diffraction system. The samples were divided into 4 cm sections in the active layer and 8 cm sections in the permafrost (total n = 77). The samples were measured while wet using the QUIXEL module, but not chemically treated prior to analysis. Samples were placed within the chamber at no more than 30% concentration of sediment. A 1.5% peptization agent ($Na_4P_2O_7$) was added to each sample to avoid particle flocculation and ultrasonicated. Each sample was measured three times with representative measurements presented here. Grain-size analysis on samples taken in 5 cm continuous segments (n = 35) from the exposed section at CS-1 was conducted on a Malvern Mastersizer X at Uppsala University with a He−Ne laser (λ = 632.8 nm) under the polydispersive model. Subsamples of c. 1−3 g were treated with 12% HCl to remove carbonates and 33% H_2O_2 to remove organic matter. Samples were immersed in 0.5% $(NaPO_3)_6$ and ultrasonicated briefly prior to analysis. Grain-size distributions were measured by three repeat measurements with mean distributions used in further analyses, after the exclusion of obvious outliers.

Although complicated by factors such as source distance and sediment availability (Újvári et al., 2016), grain-size distribution shape can help determine loess transport and depositional processes (Vandenberghe, 2013). In addition to distribution statistics and percentage of different grain size classes, the U ratio was also calculated. The U ratio is the ratio of the percentage of 16−44 μm fraction to the percentage of 5.5−16 μm fraction and is designed to exclude grains formed during *in-situ* weathering and grains transported by local saltation (Vandenberghe and Nugteren, 2001). Arguably then, the U ratio is a better indicator of the intensity of wider-scale aeolian dust suspension activity than central tendency parameters, with higher values denoting stronger winds or a more dynamic aeolian environment.

3.5. Luminescence dating, age model, and accumulation rate

Luminescence methods are ideal for constraining the timing of deposition of loess, as wind-blown sediment is normally well bleached prior to deposition (Roberts, 2008). Analyses were conducted at the Technical University of Denmark. Active layer samples are labelled as A1915# while permafrozen samples are labelled as 1915#, the postfix increasing with depth. The chronology is built using 136 luminescence dates, sampled at 2 cm vertical resolution throughout the 3 m core and pit. This very high sampling resolution reveals fine-scale changes in sedimentation rate, and the number of samples in the section is far higher than normally attempted. However, late-Holocene loess is an ideal material for rapid

equivalent dose measurements using quartz OSL, as it is normally well bleached and requires little measurement time. For dose rate measurements, use was made of recent advances in the beta counting methodology, which permit precise and accurate dose rate determination using only a few grams of material (Cunningham et al., 2018). Again, loess is ideally suited for this, because of the typically high radionuclide concentrations and relative uniformity in sediment composition within a site.

OSL measurements were carried out on quartz grains in the range 90−180 μm, extracted from ~20 g of the bulk sample using standard procedures: removal of carbonates with 10% HCl, removal of organics with 10% H_2O_2 and removal of surface coatings such as iron oxides etc. using 10% HF, with a further density separation at 2.58 g cm^{-3} using heavy liquid LST. The heavy fraction was etched for 40 min in concentrated HF to remove any remaining feldspar grains and to remove the outer alpha-irradiated rind of the quartz grains. After etching, the quartz fraction was washed in 10% HCl and several times using distilled water before drying. OSL measurements were made on typically 3−6 large (~8 mm) aliquots per sample using a Risø TL/OSL Reader Model DA-20, with stimulation for 40 s at 125 °C by blue LEDs (470 nm, ~80 mW cm^{-2}) and detection by a photomultiplier tube with a 7.5 mm Hoya U340 optical filter. Prior to blue light stimulation the grains were bleached using IR diodes (~130 mW cm^{-2}, 100 s at 60 °C) because some aliquots showed weak IRSL signals. The irradiation source (^{90}Sr) was calibrated using Risø calibration quartz (Hansen et al., 2015) and the source calibration was updated following Autzen et al. (2022). Measurements followed a standard SAR protocol (Murray and Wintle, 2000) with an extra IR bleach before the OSL step (Roberts and Wintle, 2001) and an elevated temperature blue light stimulation after each SAR cycle to reduce recuperation (40 s at 200 °C, Murray and Wintle, 2003). The initial 0.32 s of the decay curve minus a background from the subsequent 0.32 s was used for calculations (early background subtraction). Preheat and cutheat temperatures were 180 and 160 °C, respectively. Preheat temperature was based on preheat plateau tests from two samples (one active layer and one permafrost), as described below. Outliers in equivalent dose were rejected using the interquartile range criterion as proposed by Medialdea et al. (2014). Dose recovery tests were conducted on 110 aliquots from 40 samples (~every third sample).

Beta dose rates were estimated using the beta-counting procedure of Cunningham et al. (2018). Between 5 and 10 g of each sample was dried, pulverized, mixed with hot wax and cast into three disc-shaped sub-samples. After a two-week storage period to allow ^{222}Rn build-up, the beta count rates were measured for 24 h using a set of Risø low-level multi-counters (Bøtter-Jensen and Mejdahl, 1988). The conversion of beta count rate to dry dose rate requires an estimate of the relative proportions of K, U, and Th sources in the samples. These estimates come from gamma spectrometry measurements on homogenized material: 5 g per sample was combined with adjacent samples, providing one gamma spectrometry disk for every 6 samples. The lower 31 samples were combined into one gamma disk as they contained low amounts of mineral material. Measurement and analysis of HpGe gamma spectrometry followed the procedure of Murray et al. (1987, 2018). Gamma dose rates were derived from the ^{40}K, ^{226}Ra and ^{232}Th activity concentrations. This measurement strategy minimises any potential errors caused by U-series disequilibrium.

Dose rate calculations used the conversion factors of Cresswell et al. (2018), and the beta attenuation calculation of Cunningham et al. (2022), which accounts for surface-held sources of U and Th radionuclides. Dry dose rates vary very little over the 3 m profile. The major source of dose rate variation comes through the water and ice content. Water/ice content was measured gravimetrically

for each sample, with the measured water contents used to attenuate the beta dose using the calculation of Cunningham et al. (2022). For attenuation of the gamma dose, the water/ice-content measurements were first smoothed using a moving average to reflect the greater range of gamma radiation. The cosmic dose rate contribution follows Prescott and Hutton (1994), assuming a gradual sedimentation rate; an assumed alpha dose rate of 0.010 ± 0.005 Gy ka^{-1} was also included, based on Vandenberghe et al. (2008).

An age-depth model was derived from the individual OSL ages (without systematic uncertainties) using the rBacon code Bayesian model of Blaauw and Christen (2011). Output from modelling (thick = 7; acc.mean = 10; acc.shape = 1.5; mem.mean = 0.5; mem.strength = 10) was used to derive sedimentation rates obtained at arbitrary 1 cm intervals based on changing age with depth, smoothed via a 6 cm running mean. To estimate sedimentation rates for sediments only, a correction needs to be applied for ice content. Excess ice content was calculated by weight % for all samples where the ice content exceeded the natural saturation level of the sediment (mean = 39% of saturated weight). The weight % excess ice was converted to an ice volume % by assuming an ice density of 0.92 g cm^{-3} and a saturated loess density of 1.5 g cm^{-3}. Sedimentation rate values were multiplied by 100% minus the volume % excess ice to derive sediment only sedimentation rate values.

Dust mass accumulation rate (dMAR) is a more meaningful parameter than sedimentation rate for estimation of the past atmospheric dust flux to a site, and for comparisons of dust deposition across different archives and regions (Kohfeld and Harrison, 2003). However, dMAR requires estimates of sediment bulk density and the proportion of aeolian-derived material. Unfortunately, there is considerable divergence of measured dry bulk density value for loess, for example ranging from 1.2 to 1.9 g cm^3 on the Chinese Loess Plateau alone (Zhu et al., 2019). No measurements are available for Svalbard loess, and dry bulk density values will be different when measured in section, cores or in processed samples. Here we provide a very general estimate of dry bulk sediment density for the CS-1 site by heating a selection of seven representative samples from the section to 950 °C in order to dry samples and burn off organics (no carbonates are present in the loess). Resulting mean dry sediment bulk densities for the lower 110 cm of the section were slightly lower than the upper part of the section, and calculated as 1.0 g cm^{-3}, compared to 1.2 g cm^{-3} for the upper 110 cm. CS-1 core dMAR values were then calculated using the equation:

$$dMAR = SR * feol * BD$$

where SR is the sedimentation rate (m yr^{-1}), BD is the dry bulk density (g m^3) and $feol$ is the fraction of the sediment that is of aeolian origin (Kohfeld and Harrison, 2003). Based on the loss of organic material on heating to 950 °C we derive mean organic contents of 5% for material above 110 cm, and 8% below 110 cm. For simplicity, we use 110 cm as the boundary between organic contents and bulk densities also in the core. The resulting dMAR values should be treated as broad estimates due to the uncertain correlation between core and section, due to the assumptions inherent in estimating bulk density outlined above, and also due to age model uncertainty.

4. Results

4.1. Dust dynamics and loess distribution in Adventdalen

The Advent River is fed by meltwater that accompanies initial melting of snow and ice in the spring, and during warm periods in the summer (Fig. 3A+B). It transports large amounts of sediment from tributary valleys and is characterised by large fluvial bars composed of silt and sand (Fig. 3B). During autumn, as temperatures drop below freezing and meltwater production ceases, the river stops flowing completely, exposing the fluvial bars which are then 'freeze-dried' by strong and cold winds from the east/southeast (Fig.. 2B and 3C) (Bryant, 1982). These high wind speeds, oriented down valley, the freeze drying, and the relatively low amounts of snow, make the late autumn the ideal period for dust deflation to occur (Fig. 1C). The vegetation on the valley floor away from the riverbed consists of grasses, mosses, and short shrubs (Gilbert et al., 2018), acting as a dust trap for loess and also as protection against erosion (Bryant, 1982). In the summer, especially in years with less than average precipitation, crystalized salts will appear on the surface of the terrain, potentially also shielding the loess from erosion (Bryant, 1982). As winter progresses, snow
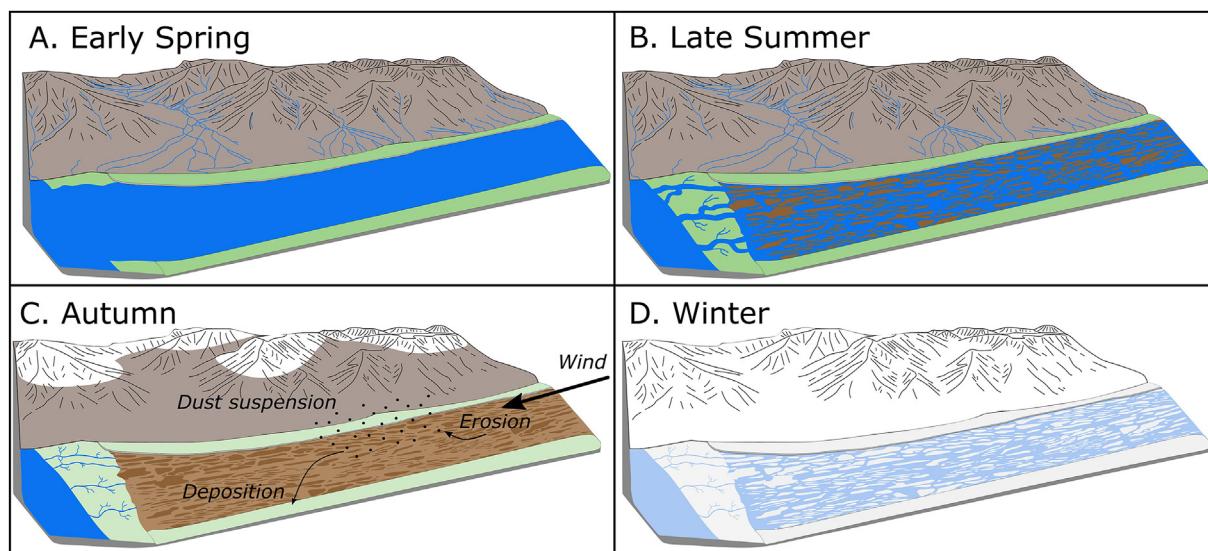
Fig. 3. A graphic rendition of seasonal changes in Adventdalen. Modified after the original figure by Gilbert et al. (2018).

accumulates and increases in thickness in the valley, restricting the transport and deposition of loess (Fig. 3-D).

Loess has been mapped along the riverbank on both sides of the river, concentrated in the lowermost part of the valley, but reducing in thickness and cover close to the delta and coast (Fig. 4). Additionally, we hypothesise that loess may be present at several other locations in the valley (hypothetical loess in Fig. 4), based on the following assumptions: 1) Watanabe et al. (2017) suggested that loess deposits thin away from the river but are still present to a distance of ~700 m. Watanabe et al. (2017) based their study on a single fan area (Fig. 4), but their findings should be applicable to the whole valley based on the relatively uniform wind-direction, topography, and vegetation cover, except for areas of obvious active alluvial fan sediments. 2) The original geomorphological map created by Tolgensbakk et al. (2000) showed pre-recent fluvial sands close to the riverbank and in areas later shown to consist of upwards of 3 m thick loess deposits (Gilbert et al., 2018; Oliva et al., 2014). Based on this and some core studies also identifying loess

(Cable et al., 2018 see Fig. 4), we propose many of these areas previously mapped as fluvial sands may also contain loess. 3) Observations of dust storms, which are frequent in the valley during the autumn, provide evidence that large parts of the centre of the valley likely experience ongoing loess deposition, where no other modern sedimentary process is obviously active. Thus, relict alluvial fans and abandoned terrace areas likely also contain some loess. However, while our map provides a working model of loess distribution in Adventdalen, we emphasise that this needs testing through more detailed field observations.

4.2. Cryostratigraphy

The cryostratigraphic core study starts at the top of the permafrost, from a depth of 98 cm. This corresponds to the depth of the active layer measured at the site, which also agrees with recent active layer thickness observations from the CALM monitoring grid at the same location (Strand et al., 2020). No cryostructures have
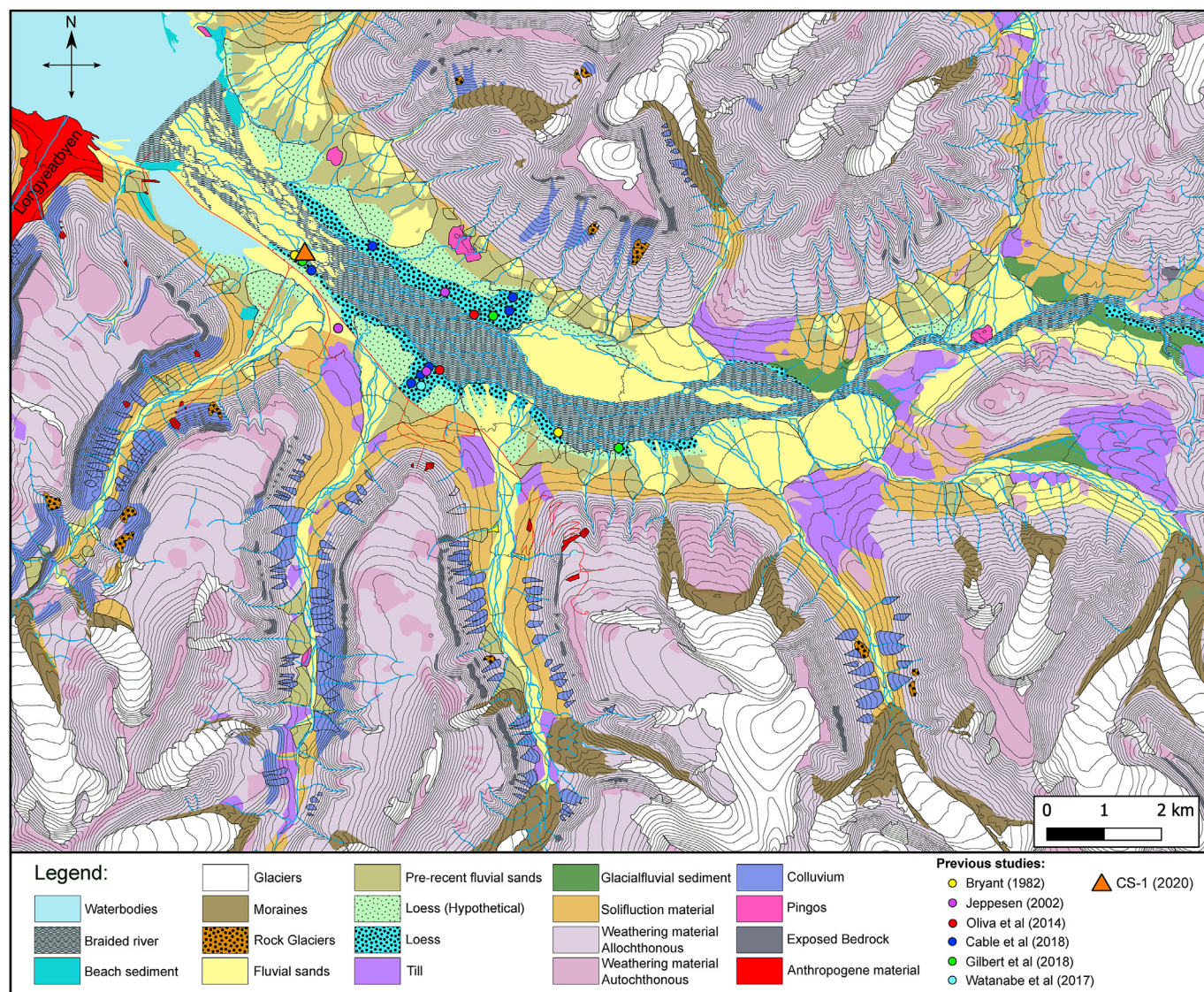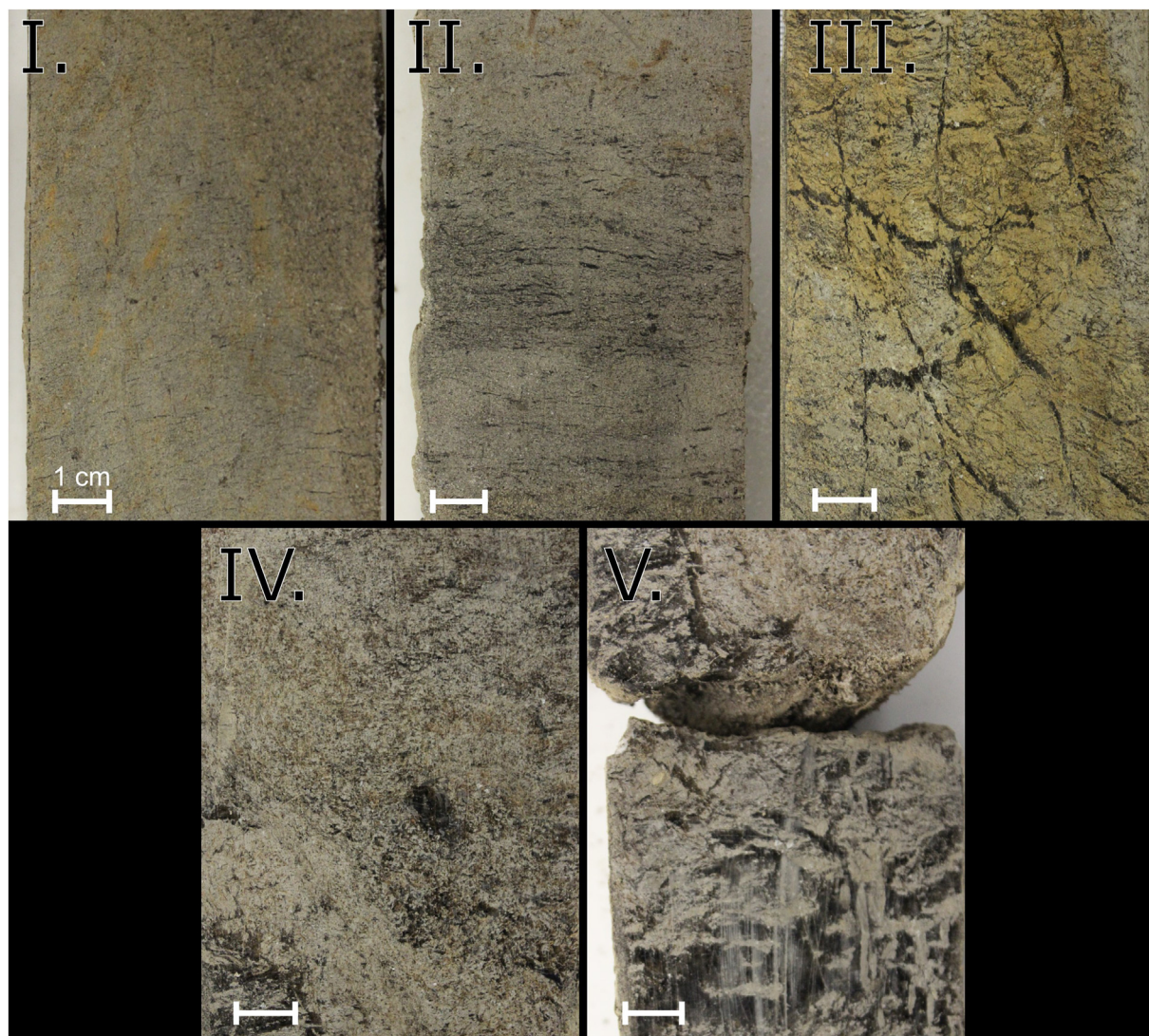

Fig. 4. Geomorphological map of Adventdalen based on the map by Tolgensbakk et al. (2000). Areas known to contain significant loess deposits are marked with dotted cyan, while areas where we hypothesise loess may also be present are marked with dotted light green.

Fig. 5. Photo examples of the main cryostructures observed in core CS1. Cryostructures are I: Pore ice (Not visible), II: Microlenticular (small ice lenses <0.5 mm long), III: Reticulate (interconnected horizontal to sub-horizontal and vertical ice veins and lenses), IV: Cryo-deformation, V: Ataxitic (near pure ice with some sediment).

been classified in the thawed out active layer due to summer sampling. The water content in the thawed out active layer is low, typically 10−20%. Examples of the main permafrost cryofeatures are shown in Fig. 5, with simplified cryostratigraphy and ice content shown in Fig. 6.

From the top of the permafrost to a depth of ~155 cm, the ground ice content is relatively low (20−50%) and occurs either as pore ice (cryostructure I) or as microlenticular cryostructures (cryostructure II), with lenses of ice <0.5 mm long. From 155 cm to ~188 cm, the ground ice content increases to 60−80% (Fig. 6), with increasing microlenticular cryostructures (Fig. 5). Below 188 cm until 223 cm, ice-free bands are observed to alternate with microlenticular pore ice structures. Here the ground ice content still varies between 60 and 80%. From 237 to 248 cm, reticulate cryostructures are visible, with ground ice contents around 60% (cryostructure III). From 248 cm to 275, sediment layering becomes obscured by a large amount of microlenticular ice (Fig. 5), with variation in ground ice content from 60 to 120% (Fig. 6). Below 275 cm to a depth of 295 cm, cryostructures are very limited and sediment layering becomes obscured by deformation structures (cryostructure IV), although with increasing ground ice content to

105−190%. The bottom of the core (below 295 cm) contains almost pure ice, with a ground ice content varying between 110 and 250%, with some sediment entrained, and is classified as ataxitic in cryostructure (cryostructure V).

4.3. Stratigraphy of the exposed section

The section at CS-1 encompasses c. 180 cm of sediment exposed down to where the section reaches permafrost (Figs. 7 and 8), locally lowered due to sediment exposure at the terrace edge. From the base to 170 cm depth, a silty peat unit is exposed, with a yellow homogenous fine blocky silt unit above. The upper boundary of the yellow silt is irregular, from 140 to 160 cm depth, above which is a sequence of dominantly grey-purple homogenous silt units, with occasional cm-thick orange bands. The grey-purple bands have numerous vertical orange streaks. These bands are cut at 130 cm depth by an infilled wedge of light-coloured silt (Fig. 8). Between 110 and 50 cm, a light-yellow orange silt unit is exposed with occasional fine sandy mm-scale bands that become more frequent and sandier towards the top. Between 75 and 70 cm a faint orange band is visible. At 50-45 cm, a prominent cross bedded sand layer is
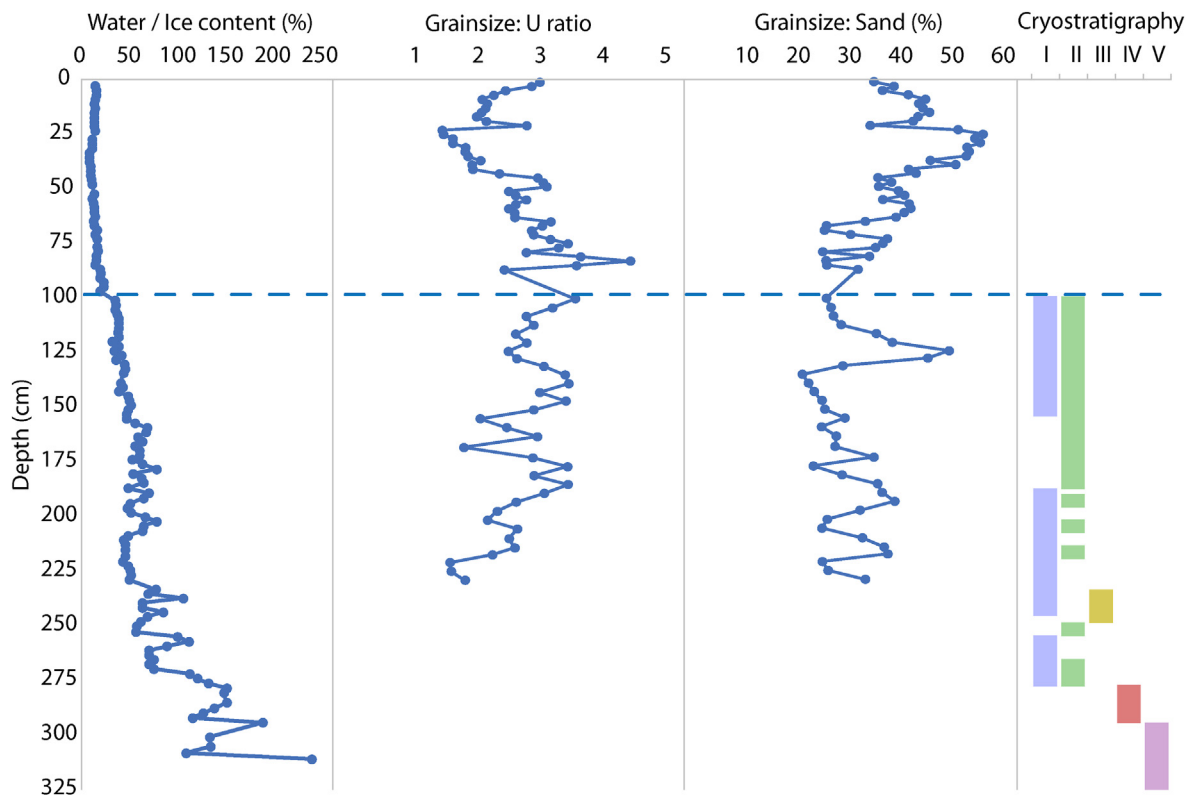
Fig. 6. Water and ice content (dry weight %), grain-size indices, and cryostratigraphy at core and pit CS-1. Grain size only available to a depth of 229.1 cm because of significantly increased organic content at greater depths. Cryostratigraphy I: Pore ice (Not visible), II: Microlenticular (small ice lenses <0.5 mm long), III: Reticulate (interconnected horizontal to sub-horizontal and vertical ice veins and lenses), IV: Cryo-deformation, V: Ataxitic (near pure ice with some sediment). See Fig. 5 for examples. The blue line denotes the transition from active layer above to permafrost below.
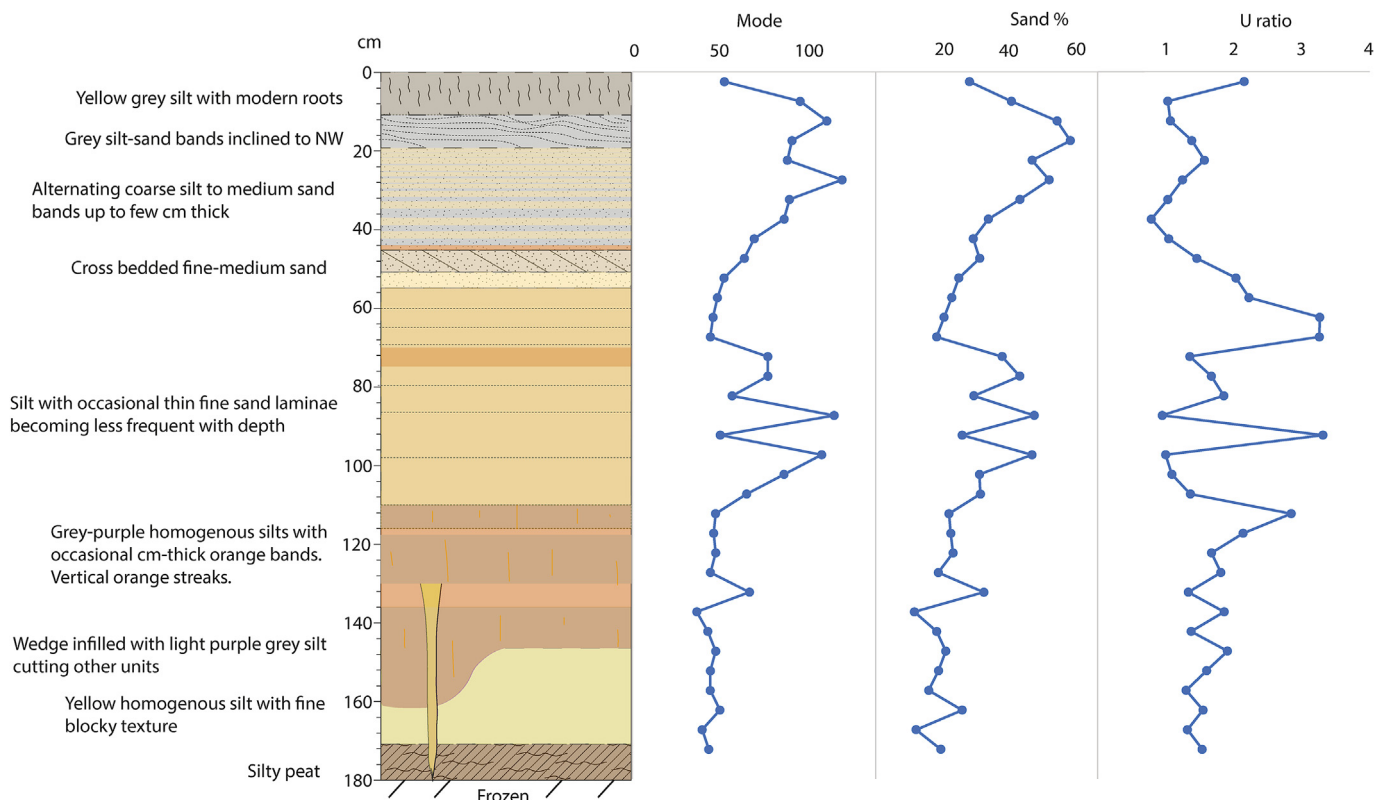
Fig. 7. Stratigraphic log of the sample section at CS-1. Mode (microns), sand content (%) and U ratio by depth are also shown.
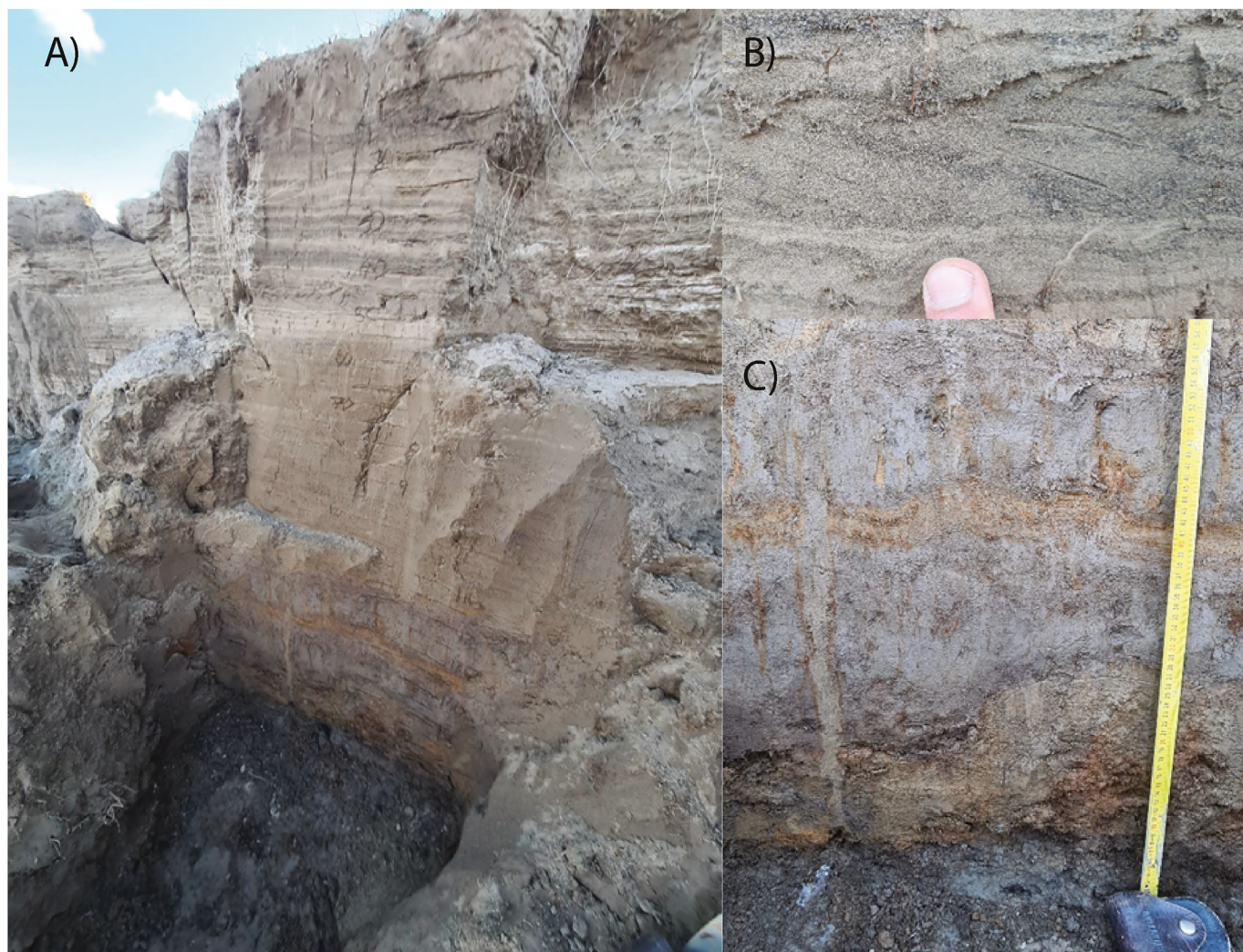
Fig. 8. Pictures of section CS-1. A) shows overview of whole section, while B) shows cross bedded sediments in the upper part of the section, and C) shows infilled wedge in lower part of section.

clearly expressed, with sharp erosional contacts and with the beds dipping down river valley to the NW (Fig. 8). Between 45 and c. 20 cm, a banded silty fine sand unit is exposed, with dark grey sands alternating with light yellow silts at cm to mm scale. Between 20 and 10 cm, sub-horizonal wavy, banded silty sands are exposed. A massive grey silty loam with numerous modern roots is exposed in the top 10 cm of the section.

4.4. Grain size analyses

In the samples measured from the core and active layer pit, grain size shows a general increase upwards, albeit with considerable variability (Fig. 6). Mean values are all in the silt range, but with peaks in sand content attaining 50% at 23−40 and 120−130 cm. By contrast, for these two intervals, U ratio values show decreases in coarse silt relative to fine silt abundance. Peaks in U ratio occur in the top 10 cm of the section, and approximately at 40−50, 60−90, 90−110, 130−150, 175−195, and 210−218 cm depth. Where not associated with sand content increases, this implies an overall coarsening of the silt component, rather than a sudden influx of sand, as occurs at 23−40 and 120−130 cm. Grain size distributions in the core and pit typically show two broad patterns in CS-1 samples, as typified in the two examples in Fig. 9; the example
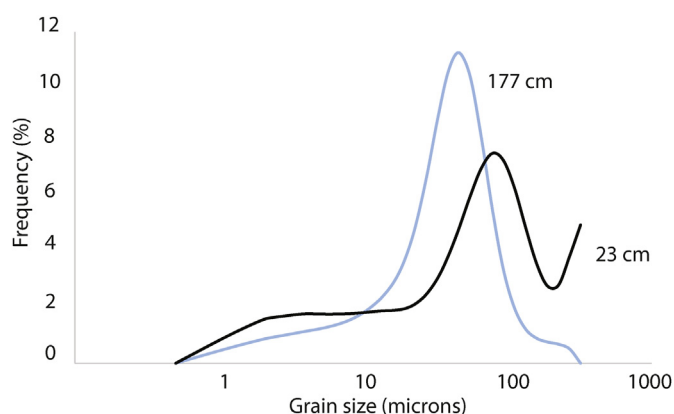
Fig. 9. Typical grain size distributions from CS-1 core and active layer pit. Values denote depth of samples (Fig. 6).

from 23 cm reflects a typical distribution for the sandier interval between 23 and 40 cm, and the distribution from 177 cm reflects the majority of other sediment in the core.

Samples measured from the exposed section (Fig. 7) show similar patterns with depth to those in the core and pit samples, but

section samples were taken at a larger sampling interval, and some differences are also observed (Fig. 10). The upper 55 cm is dominated by coarser modes and higher sand content, while between 70 and 110 cm there are variations between silt- and sand-dominated sediments. Elsewhere, modes are in the silt range with sand contents around 20%. U ratios follow a different pattern to sand contents, as with the core and pit samples. Peaks in U ratio occur in the upper 10, 65, 90 and 110 cm depth (Fig. 7). A tentative correlation between the pit/core and section is shown in Fig. 10, and outlined in the Discussion.

4.5. Luminescence data, age model and sedimentation/mass accumulation rate

The purity of quartz samples was investigated by examining the aliquot's sensitivity to infrared stimulation. Most quartz extracts did not exhibit any significant IR signal (Fig. 11E). However, a small group of samples did show a substantial signal after infrared stimulation, even after having been etched twice with 40% HF (Fig. 11F). This was most likely caused by feldspar inclusions within the quartz crystals, and so a double SAR protocol was applied (Roberts and Wintle, 2001). The quartz OSL signals are dominated by a strong fast component (inset Fig. 11C and D) and we were able to remeasure points on our dose response curves, as evidenced by recycling ratios close to unity (Fig. 11A). A dose recovery test was measured on 110 aliquots from 40 samples, i.e. roughly every third sample, and the results are summarized in a histogram (Fig. 11B), with mean dose recovery of the samples being 1.03 ± 0.01. Two preheat plateau tests were also conducted on two separate samples (Fig. 11G–J). Fig. 11G and I illustrate that while the recycling ratio of A91541 is comfortably within the 10% limit for a range of preheats, 191576 shows a slightly higher degree of variation. Fig. 11H and J
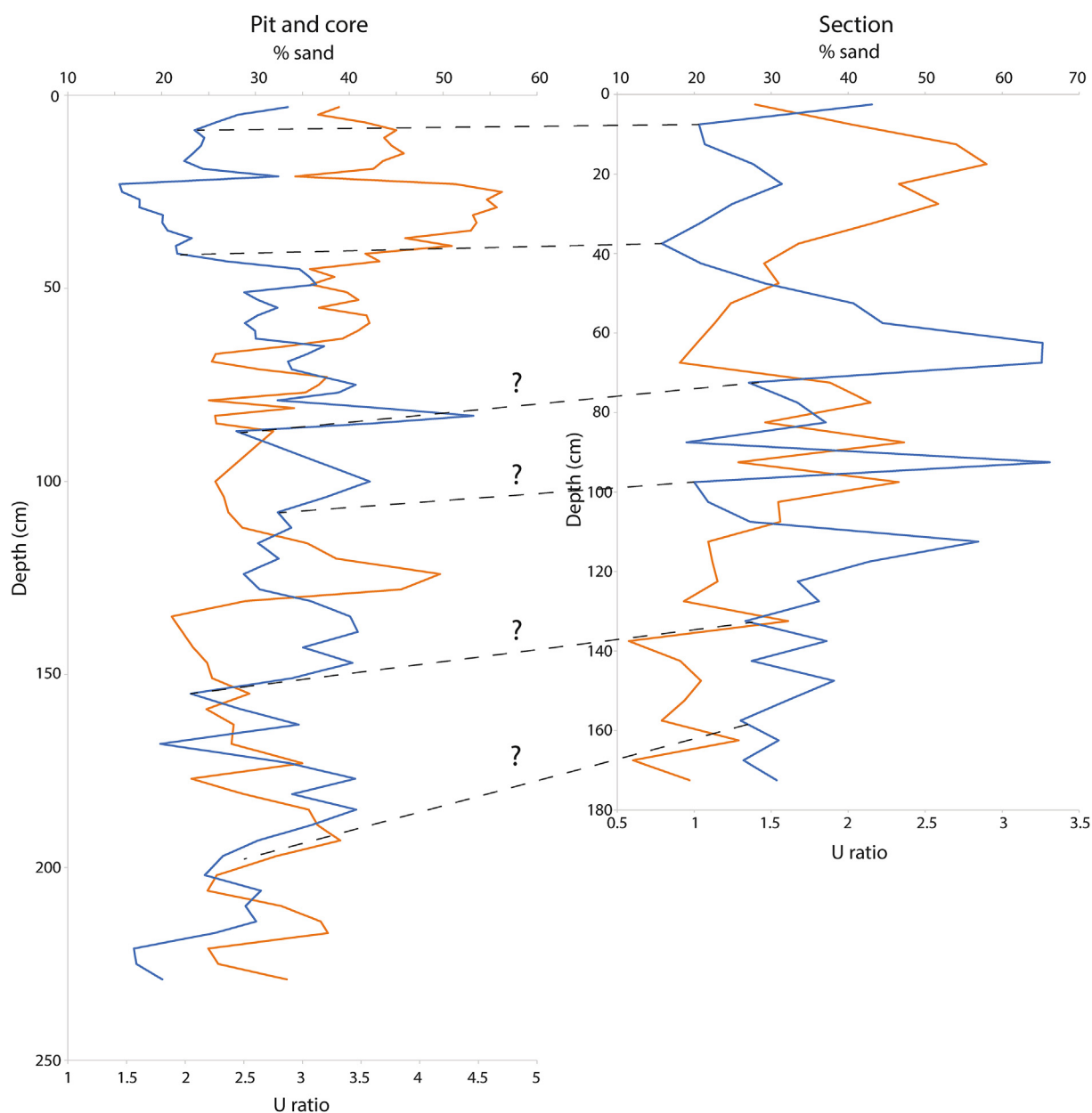
Fig. 10. Sand content (orange) and U ratio (blue) by depth for the pit/core and section at CS-1. Tentative correlations between layers are shown by dashed lines, and explained in the text.
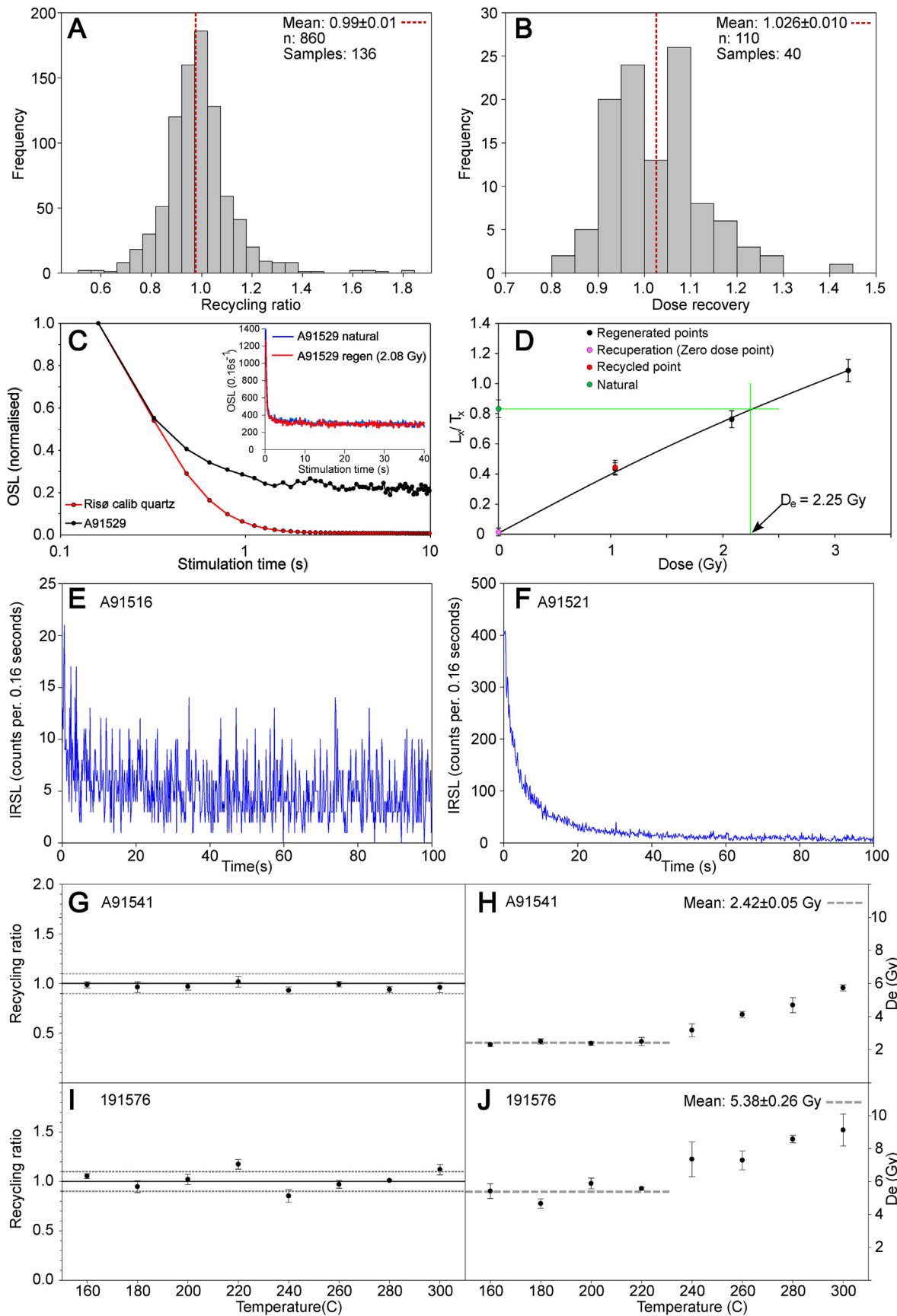
displays the equivalent dose (D_e) variation as a function of preheat temperature. An increase in D_e is recognizable at a temperature of 240 °C in both samples; this is due to thermal transfer. The averages of the first four preheat temperatures (160−220 °C) are plotted on Fig. 11H and J, with mean values of 2.52 ± 0.05 Gy and 5.60 ± 0.27 Gy respectively.

Fig. 11C shows an example decay curve from a representative sample (A91529), with a strong fast component present for all quartz extracts. Fig. 11D shows an example sensitivity-corrected growth curve A91529. The recycling ratio measurements (Fig. 11A) were conducted as a part of the equivalent dose estimations. A total of 136 samples were analysed based on a total of 860 aliquots with a minimum of 3 and a maximum of 12 aliquots measured for each sample. The mean recycling ratio for the samples was 0.99 ± 0.005, lying well within 10% of unity. Full dose rate and luminescence data are shown in Supplementary Tables S1-4.

Fig. 12 illustrates radionuclide concentration variation as measured from individual samples (beta buttons) and homogenized sample intervals (gamma discs). The beta dose rates as well as the radionuclide concentrations of ^{238}U, ^{226}Ra, ^{210}Pb, ^{40}K and ^{232}Th are plotted against depth. There is very little variation in the radionuclide concentrations, but some instances of change are noted. ^{238}U changes very little with depth and shows no obvious difference between the active layer and permafrost. A slight increase in the concentration of ^{238}U is observed at 166−176 cm, increasing with depth to 218−229 cm. A similar pattern is observed in the concentrations of the other radionuclides. The concentrations of ^{40}K and ^{232}Th are almost identical in the pattern they exhibit, with an overall slight increase in concentration with depth. The dry beta dose rate contains almost no outliers and changes very little with depth.

Disequilibria in the U-series are present in the samples and informative. Low ^{226}Ra/^{238}U ratios (Active layer: 0.86 ± 0.03; Permafrost: 0.93 ± 0.04) may reflect a disequilibrium in the fluvial source material, where radium is mobilised in water and depleted from the sediment fraction. Equilibrium is being re-established in the permafrost on a timescale governed by the half-life or ^{226}Ra (~1600 yrs).

The active layer can broadly be divided into three segments based on luminescence ages and the derived changes in sedimentation rate (Fig. 13A). Due to the relative constancy of the dose rate (Fig. 12), similar patterns are also seen in equivalent dose (Fig. 13B): 1) 0−20 cm, where samples display ages between c. 150 and 400 a, 2) 20−50 cm, where all sample ages cluster around c. 600−700 a, and 3) >50 cm, where the ages vary from 800 to 1100 a with slightly increasing age with depth. At the transition between the active layer and the permafrost, an increase in age to c. 1200−1300 a is observed in the first permafrost samples. Below this, the age of the permafrost samples broadly increases with depth to around 250 cm. Below 250 cm, the samples begin to exhibit a higher degree of age variability. A considerable increase in age is noticeable from a depth of 275 cm. After an initial increase in uncertainty of each sample age at c. 190 cm, uncertainty also increases rapidly from 275 cm and downwards. In general, the age model uncertainty (95%) in the dominantly loess part of the core (down to 275 cm) ranges from ±30 yrs (top) to ±100 yrs (265 cm).

Fig. 13A shows the age-depth model and the derived sedimentation rates. The highest sedimentation rates occur in the upper part in the top of the active layer, where rates exceed c. 0.3 cm per year. Below the active layer boundary, maximum rates generally do

not exceed 0.15 cm per year, and slightly increase up core, in line with decreasing ice contents. However, between 165 and 215 cm a broad sedimentation rate peak occurs, with rates up to c. 0.25 cm per year. There are numerous peaks in sedimentation rate down section, although below c. 250 cm the scatter in the ages means that sedimentation rate peaks over this interval are much more uncertain. Analysis by age (Fig. 14) reveals the timing of these multiple peaks in sediment accumulation rate. Broadly, these intervals correspond to the last c. 250 yrs, as well as 600−700, 750−900, 1050−1200, 1400−1600, 1900−2450 and possibly 2700−3000 a, with maximum age model uncertainty ±100 yrs for the oldest peaks, and <±50 yrs for younger peaks. As expected, changes in dMAR coincide with sedimentation rate changes, but show slightly different peak heights, due to differences in estimated sediment dry bulk density and organic content down core.

5. Discussion

5.1. Late Holocene permafrost reconstruction

Based on the CS-1 core and active layer sediments we reconstruct the late Holocene permafrost environment. The permafrost is characterised by a very clearly decreasing ground ice content up through the core (Fig. 6). At the bottom or the core, there is large variation from 100% to 250% in the measured ground ice content, whereas above 225 cm there is distinctly less variation, typically between 40 and 70%, and ending with around 40% at the top of the permafrost. This most likely reflects the accumulation of sediment increasingly above the riverbed and the underlying fluvial sediments, and seems to correspond to generally higher loess sedimentation rates up core (Fig. 13). The top of the permafrost down to 237 cm is dominated by pore ice and microlenticular cryostructures, which are typical of syngenetic permafrost formation (French and Shur, 2010). From 237 to 248 cm reticulate cryostructures are observed, which are usually associated with epigenetic permafrost formation (French and Shur, 2010). Often, reticulate cryostructures are believed to develop through desiccation and shrinkage during sediment freezing, while moisture migrates towards an advancing freezing front (French and Shur, 2010). However, from 248 to 275 cm syngenetic permafrost formation is again most likely, due to the dominating pore ice and micro lenticular cryostructures. Deformation structures between 275 and 295 cm are most likely caused by cryoturbation or by formation/intrusion of epigenetic ice from below. A change to ataxitic ice at the bottom of the core from 295 cm to 320 cm (Fig. 6) can be interpreted to denote the boundary between loess and the underlying sediment, as ataxitic ice structures are generally considered indicative of epigenetic permafrost (French and Shur, 2010). Ataxitic cryostructures develop where sediment grains or aggregates are suspended in ice; in many cases it forms in the intermediate layer at the top of permafrost (Gilbert et al., 2016). Potentially, this cryostructure corresponds to the peaty loess layer seen in at the base of the section (Fig. 7).

Permafrost growth is believed to have begun at the same time as aeolian sedimentation (Gilbert et al., 2018) and this may have concentrated water at the boundary between fluvial and aeolian sediment, as permafrozen sediment functions as an aquitard (French and Williams, 2017). The high ice content may also have led to deformation, simply due to the secondary epigenetic intrusion of ice into the sediment (French and Williams, 2017; Watanabe et al.,

Fig. 11. Results of luminescence analyses. A: Recycling ratio, B: Dose recovery ratio, C: Normalised decay curves of Risø calibration quartz and A91529, showing presence of fast component. Inset shows natural and regenerative dose decay curves of A91529. D: Equivalent dose determination of sample A91529, E and F: IRSL signal from A91516 and A91521, G−J: Preheat plateau recycling ratio (G and I) and equivalent dose (De) (H and J) for samples A91541 and A91576.
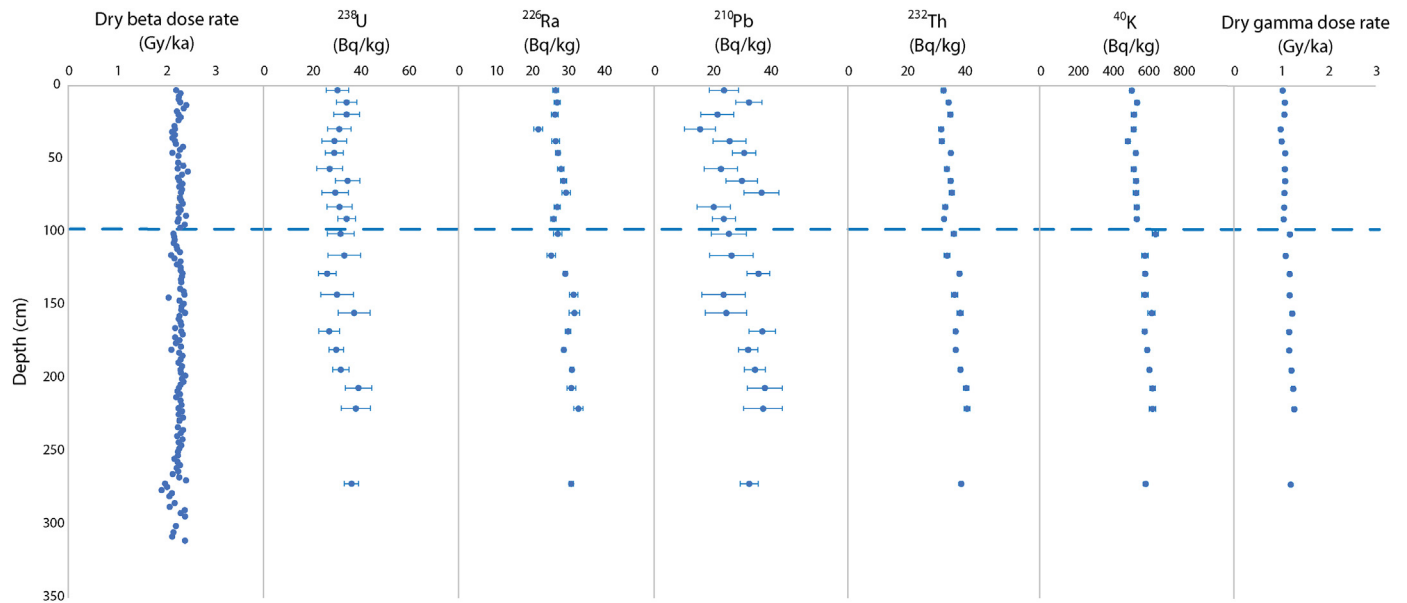
Fig. 12. Infinite matrix dry beta and gamma dose rates compared. As gamma discs need ~5x the amount of material than a beta button, gamma discs are combined from ~5 samples, depending on the amount of available material. The deepest gamma disc covers 31 samples as less material was available. The blue line indicates the boundary between permafrost and active layer.
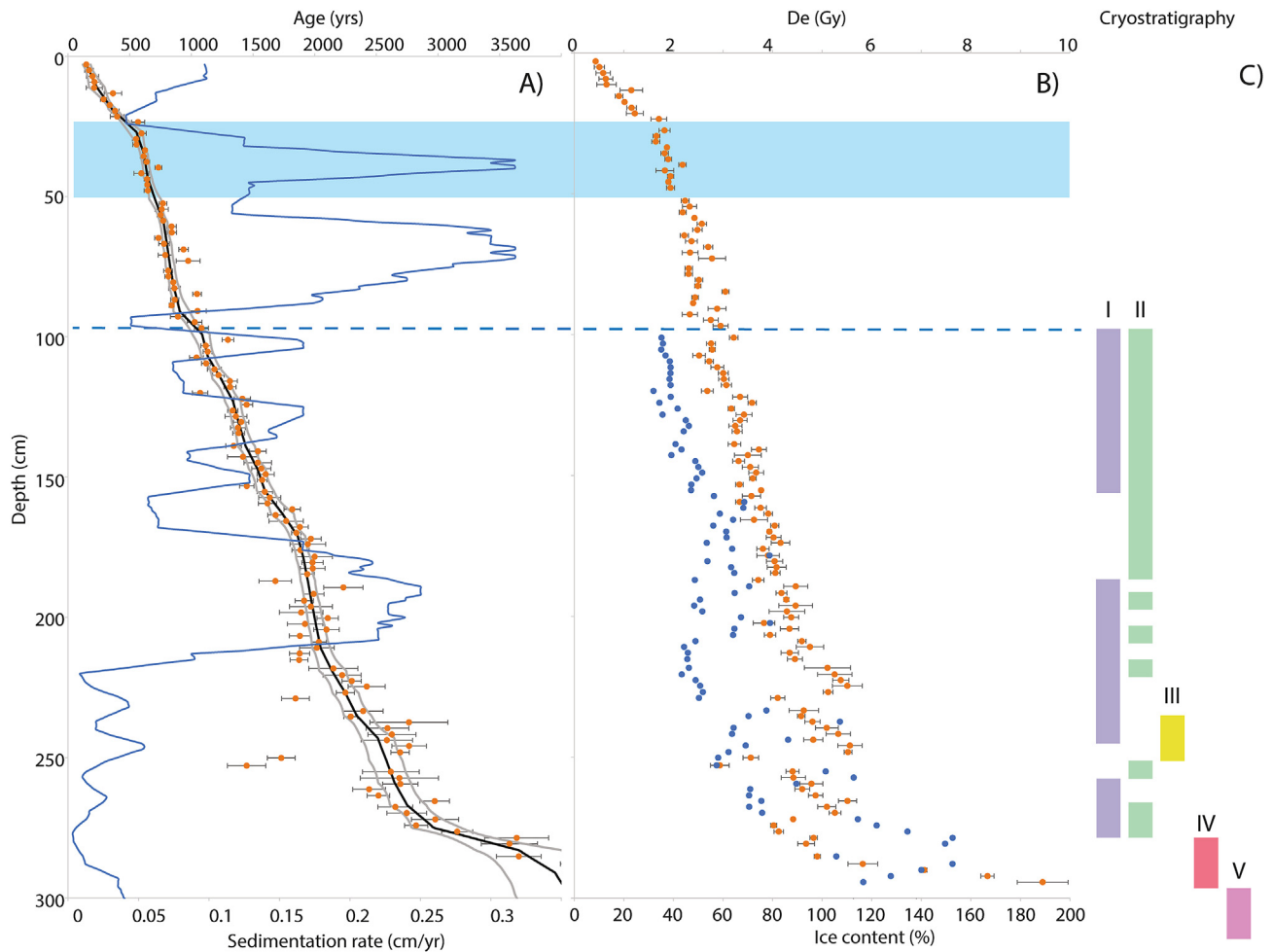
Fig. 13. A) OSL age versus depth, age model mean (black), max and minimum (grey) 95% confidence intervals and derived sedimentation rate (blue) for CS-1 active layer and core. B) shows equivalent dose (D_e) and ice content (blue dots) with depth. C) denotes major cryostructures identified by depth (Fig.. 5 and 6). Blue dashed line represents bottom of the active layer above the permafrost, and blue shaded area shows interval bracketed by jumps in D_e and age.
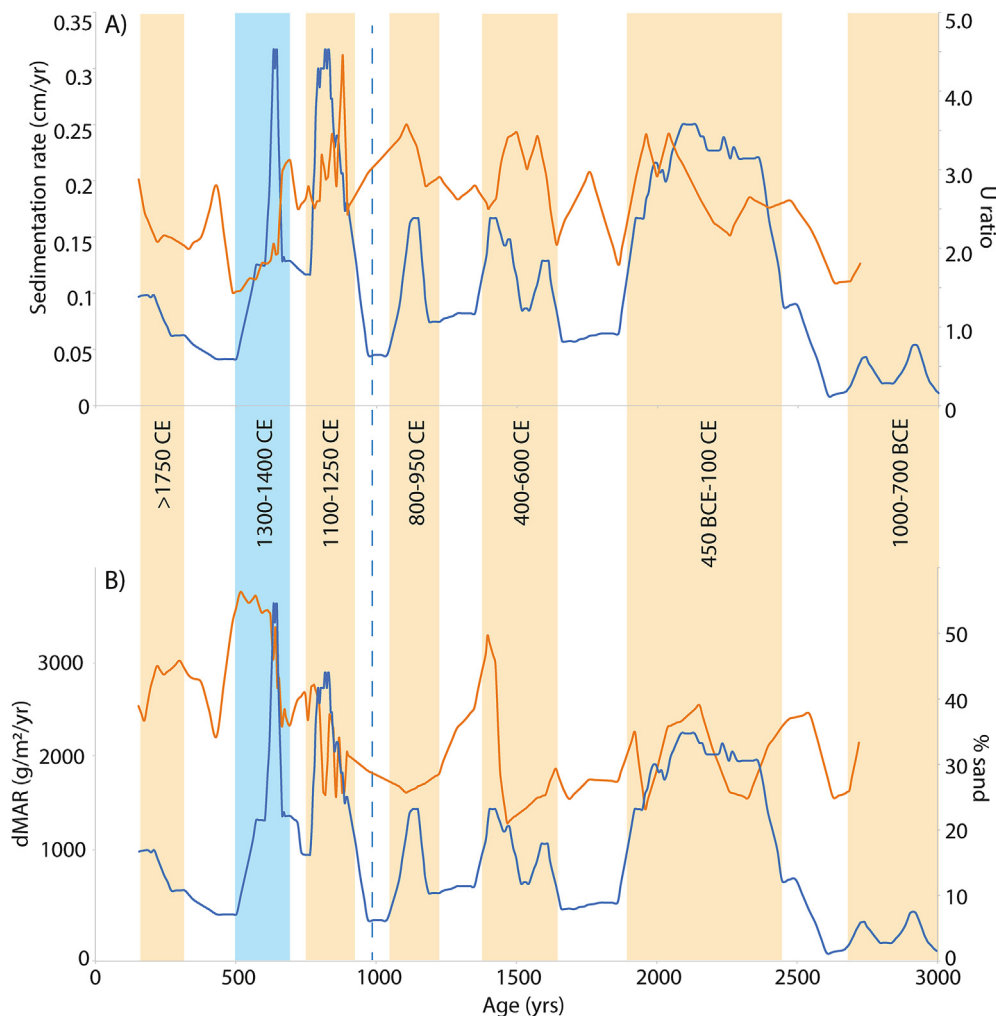
Fig. 14. A) Sedimentation rate (blue line) and U ratio (red line) and B) dust mass accumulation rate (dMAR; blue line) and sand content (red line) by age. Dashed blue line divides the present active layer to the left from the permafrost to the right, while the blue shaded area shows interval with little increase in age or D_e with depth, and with sudden changes in D_e and age either side (see Fig. 13A). Yellow shaded intervals reflect broad time periods when peaks in dMAR correspond to peaks in U ratio (higher coarse silt content). Age ranges marked on the shaded intervals reflect the approximate time periods of these high sediment accumulation rate events.

2017). However, there is a clear need for more studies of cryostructures as well as sediment properties at multiple sites along the valley to fully test this. Overall though, the main part of the permafrost studied down to 295 cm indicates clear syngenetic permafrost formation, with a 11 cm thick section 237-248 cm indicating epigenetic permafrost formation. Epigenetic permafrost formation also occurs just prior to the start of loess formation at the bottom of the studied core and section.

Based on the core cryostratigraphy and grain size, section stratigraphy and grain size, and core and pit luminescence ages (Figs. 6, 7, 10 and 13) we suggest that aeolian silt deposition began around 3000−3500 a at c. 275 cm depth, but was likely initially associated with peat growth until full loess deposition occurred later at around 2500 a (c. 220 cm). Our estimate of initiation of loess sedimentation fits well with the timing of 3000 a proposed in Gilbert et al. (2018), after fluvial incision exposed terrace surfaces in the valley that were able to host loess accumulation. Fluvial sedimentation preceding this loess formation occurred after progradation of a Gilbert delta down valley during the early-middle Holocene, with relative sea level fall driving incision and terrace formation (Gilbert et al., 2018). Luminescence ages from below c.

290 cm in the core increase dramatically to between 7500 and 4000 a, although these are hard to interpret due to scatter, presumably driven by ice contents and possibly cryoturbation during epigenetic ice growth (Fig. 13). Loess deposition appears to have been a relatively continuous process since c. 3000 a, as there are no significant jumps in age with depth until c. 50 cm deep (c. 600−700 a) (Fig. 13). This change coincides with a large increase in sand content and suggests either extensive niveofluvial reworking of loess, or some other aqueous sedimentation, as shown in the section stratigraphy (Fig. 7). Above 20 cm depth, primary loess sedimentation is again recorded from 350 a.

5.2. Sedimentary environment

Broadly, the main sedimentary features in the studied section can be interpreted to show five broad changes in sedimentary environment (Figs. 7 and 8).

1) 180-170 cm: peat development with aeolian silt input;
2) 170-110 cm: typical primary aeolian loess sediment (similar to grain size distribution example '177 cm' in Fig. 7);

3) 110-55 cm: loess deposition continues but with intervening thin sandier bands (max 1 cm), perhaps indicating periodic surface reworking;

4) 55-10 cm: an episode of subaqueous sedimentation or niveo-fluvial reworking is evidenced by cross bedding, alternating sand-silt banding, wavy bedding, and high sand contents (Fig. 7). These features are not compatible with typical, silty, primary loess (Schaetzl et al., 2018);

5) 10-0 cm: primary, undisturbed aeolian loess.

Bryant (1982) noted silt-sand banding in the upper part of what he defined as loess in Adventdalen, and attributed these bands as due to the formation of salt crusts on loess deposits acting to preferentially retain coarser particles, with subsequent vegetation development promoting retention of fine grains. Breakdown of that stratification lower down profile was attributed to proximity to the permafrost table and inhibition of drainage (Bryant, 1982). However, the results we present suggest that there are more fundamental differences in the sedimentary environment shown up the studied section, at least at CS-1, and this banding may rather be reflective of sub-aqueous deposition or reworking for this part of the sequence. Notably, the change to finer grain sizes as the banding disappears cannot be explained by inhibition of drainage, while observed sandy cross bedding (Fig. 8) is incompatible with loess depositional processes. The exact process generating the sediments between 10 and 55 cm in the profile is unclear, but a number of possibilities can explain the features. The cross bedding suggests transport from SE to NW, in line with Advent River flow direction. However, the dramatically enhanced water levels in the Advent River required to generate this cross bedding seem implausible given the width of the valley (c. 1 km), historical observations of low water levels even in flood, and the relatively high location of this part of the section above the present water level. Alluvial fan development from the side valley Endalen (Fig. 1B) may also explain the sediments over this interval. However, this process would be hard to reconcile with the geomorphological evidence that sometime during the Late Holocene, river flow from Endalen was diverted towards NW to the Isdammen area by the sediment accumulation at the CS1 site, extending as a peninsula in the down valley direction over the lower Endalen fan. Another explanation is extensive niveofluvial reworking of previously deposited loess, as is currently often seen in Adventdalen during spring snow melt. This would, given the thickness of the sandy sediment layers shown in the section (Figs. 7 and 8), reflect a substantial difference in local snow-melt environment over this interval, as compared to remaining 3000 yrs of loess accumulation. However, some evidence of loess surface reworking is also seen between 110 and 70 cm in the occasional thin sandy bands. While the clear >5 cm-thick ripple cross bedding at 45−50 cm implies water depths of >5 cm (Allen, 1962), at least locally, we deem niveofluvial reworking the most likely explanation for the features over this interval.

Despite this thick sandy interval in the sequence, we interpret the sediment above 10 cm and below c. 55 cm in the section at CS-1 as true, primary in situ loess (Fig. 10). Grain-size distributions for much of the sediment bracketing this interval (Fig. 9) are consistent with coarse to medium silt dominated loess with a finer silt to clay tail, typical of relatively source-proximal loess deposits (Stevens et al., 2022). Between 70 and 110 cm, the mostly homogenous silty loess contains occasional max 1 cm thick sandy bands, potentially indicative of local niveofluvial surface reworking. Below 110 cm there is considerable colour variation between orange and purple grey, with mottling and orange streaks present (Figs. 7 and 8), consistent with gleyed Arctic soil development (Bryant, 1982). We interpret these colour changes to reflect changes in the

thickness of the active layer during loess accumulation, and hence changes in water availability and oxidation-reduction state, with water logging at the permafrost table. The sediment infilled wedge feature at 130 cm that cuts to the base of the exposure (Figs. 7 and 8) may be a syngenetic sand wedge, or possibly an ice wedge cast. At the base of the section, peaty silt is exposed, suggesting that organic rich, peaty loess deposits formed prior to full loess accumulation, with enhanced peat formation perhaps facilitated by the lower terrace level and proximity to the water table.

Comparison of grain-size indices between the active layer/permafrost and the sediment section (Fig. 10) is complicated by the different sampling interval, sampling technique, instrumental and analysis methods used. However, some observations are possible. Both the pit/core and section show substantial and rapid increases in sand content in the upper part of the sequences, as well as increases in U ratio in the uppermost part, and at multiple points down section (Fig. 10). Overall sand contents and U ratios are comparable, and apart from the sandy intervals, show values typical for source-proximal loess. Tentatively, we suggest that the interval of high sand content between 20 and 50 cm depth in the active layer at CS-1 correlates to the part of the section between 10 and 55 cm, interpreted as reworked (Fig. 10). This interpretation is supported by the luminescence results that show identical ages between 20 and 50 cm deep, with jumps in age above and below (Fig. 13). This pattern suggests that an abrupt change in sedimentary environment occurred, likely associated with reworking, at least locally at the CS-1 site. The precise point in the core where the shift to peaty loess shown at the base of the section (Fig. 6) occurs, is not entirely clear, but may coincide with the increased organic contents observed at c. 200−225 cm depth (Fig. 10). This also coincides with a shift to more variable OSL ages with depth, potentially due to dosimetric effects from high organic contents and higher ice content (Fig. 13).

5.3. Validity of ages and age model

Quartz from the permafrost and active layer is fast-component dominated, yields bright, reproducible signals, does not show high rates of aliquot rejection, and passes all relevant internal tests of the assigned SAR protocol (Fig. 11). As such, we suggest that there is good reason to be confident in the accuracy of the ages. The relatively low scatter in equivalent doses in the upper 250 cm of the core suggests that partial bleaching is not occurring, and reinforces the model of loess sedimentation occurring primarily during autumn (Fig. 3), rather than during the polar night in winter. The increased scatter in equivalent dose below c. 200 cm depth (Fig. 13) is due to the larger and more variable ice content in the core, which causes a more variable dose rate. The ages show far less scatter (Fig. 14), which implies that the estimated dose rates are accurate. The novel dose rate strategy used here is very successful. The range of beta radiation in sediment is small (~2 mm), so we used a beta counter to measure the beta dose rate for every sample: the method is precise, cheap, and uses only a few grams of material. Gamma dose rates were derived from gamma spectrometry measurements on a smaller number of (combined) samples. The range of gamma radiation in sediment is much greater (~30 cm), so estimates at high sampling resolution are not required. Gamma spectrometry measurements indicate a small degree of disequilibrium in the U-series, but our dose rate strategy ensures that this does not cause an error in the estimated dose rate. The excess ^{238}U does not affect the gamma dose, because the main gamma emitters are in the middle of the chain (^{226}Ra and progeny); thus the measured ^{226}Ra is used to estimate the gamma dose rate. Excess ^{238}U does however increase the beta dose rate, but also increases the measured beta count rate proportionately, and so the estimated

beta dose rate remains accurate.

While the cryostructures are dominantly microlenticular, and likely syngenetic, the high and spatially heterogeneous ice content will result in dosimetric effects that hinder estimation of true effective burial water content. Furthermore, below c. 295 cm there is a change to ataxitic ice indicating epigenetic permafrost, which will change dose rate through time. This also complicates assignment of ice content values for this depth for dose rate calculation. This is a limiting factor in dating of ice-rich sediments using luminescence, especially if that ice may be epigenetic. Furthermore, below 275 cm, cryoturbation or intrusion of epigenetic ice from below may also have led to physical movement of sediment and caused the age inversions seen over this interval (Fig. 13). Overall though, the relatively consistent age increases with depth for the rest of the studied interval (Fig. 13) add to the confidence in the accuracy of the ages for loess deposition.

Age models by design contain assumptions about sedimentation rates that can compromise their accuracy. However, the consistent age increases with depth for most of the data here increase confidence in the output of the age model, as does the very high sampling resolution employed in the study, as each peak is based on several ages. The timing and relative height of derived sedimentation rate peaks should be broadly accurate, but especially for relatively rapid sedimentation rates, where age increases with depth are small and within individual luminescence age errors, the absolute values of sedimentation rate may only be generally accurate (Perić et al., 2019). Nonetheless, the broad timing of our sedimentation rate peaks is consistent with the luminescence ages themselves (Fig. 13), and the peaks in sedimentation rate closely align with the peaks in the U-ratio, which independently suggests the sedimentation rate peaks are real, and have a common driver as silt-size changes. As such, we argue that our uniquely detailed dating means that the sedimentation rate by age function (Fig. 14) accurately reflects the timing of changes in dust and other sediment accumulation rates in the studied sediments of the permafrost and active layer.

5.4. Late Holocene environmental change and the causes of dust activity in Adventdalen

The high sampling-resolution luminescence-based age model for CS-1 permits analysis of loess sedimentation and dMAR over the last 3000 yrs with 95% confidence intervals of 50−100 yrs, allowing previously unattained detail in reconstruction of dust accumulation (Fig. 14). Although there is considerable variability, there is a tendency to somewhat increased sedimentation rate through time (Fig. 14), corresponding also to decreasing ice contents in the permafrost (Fig. 13). This may suggest a gradual increase in sediment availability, increasing dryness due to sediment accumulation lifting the site above the river or wider aridification, or more wind activity over the last 3000 yrs. This general increase in loess accumulation rate coincides with drops in snowline and glacier advances on Svalbard, especially between 2500 and 500 a (Farnsworth et al., 2020), and with decreasing Fennoscandian summer temperatures (Sejrup et al., 2016).

Superimposed on the long-term trend are 6−7 short phases of enhanced sediment accumulation rate (Fig. 14). We propose that six of the seven identified phases correspond to enhanced primary dust activity, while the penultimate phase (sedimentation rate = 0.3 cm yr^{-1}) has been affected by reworking, likely under local niveofluvial conditions (Fig. 14). The timing of this penultimate phase (c. 600−700 a) corresponds to the proposed onset of the Little Ice Age (LIA) on Svalbard, around 1250 AD (Svendsen and Mangerud, 1997), during which time polar airmass penetration significantly increased (Balascio et al., 2018). While the exact nature

of the LIA on Svalbard is debated, the phase of sandy sedimentation/reworking identified at CS-1 coincides with the first of two possible glacial advances over the LIA (Werner, 1993; Humlum et al., 2005; Røthe et al., 2015; van der Bilt et al., 2015; Farnsworth et al., 2020), as well as sea ice expansion around Svalbard (Grinsted et al., 2006; Müller et al., 2012) and reduced summer time temperatures (D'Andrea et al., 2012). It is plausible that climatic changes and periods of ice advance during the LIA may have promoted the niveofluvial reworking or changes in depositional environment at CS-1 over this interval. However, the wider climatic causes of this ice advance are disputed, with low temperatures (Humlum et al., 2005), enhanced winter precipitation (D'Andrea et al., 2012), and long-term adjustment of glacier extent to persistent cold climate from 1800 a (Balascio et al., 2018), all being suggested. As such, it is currently difficult to assign a wider forcing agent to the sandy interval at CS-1 and indeed the LIA ice advances may not even be the largest of the Neoglacial (Farnsworth et al., 2020). Furthermore, the extent to which this is only a local event at CS-1, with no direct link to wider climate variation, remains unclear. More detailed climate proxies are required for terrace sediments, as well as more extensive analyses of loess records, to identify the extent of this episode in Adventdalen.

We identify 5−6 phases of enhanced primary dust deposition at CS-1, with the highest sedimentation rates exceeding 0.3 cm yr^{-1} (dMAR = 2900 g m^{-2} yr^{-1}) around 750−900 a (Fig. 14). Another large peak in sedimentation rate occurs at 1900−2450 a (0.25 cm yr^{-1}; dMAR = c.2000 g m^{-2} yr^{-1}), with another three peaks showing slightly lower rates of around 0.1−0.2 cm yr^{-1} (dMAR = 1000−1200 g m^{-2} yr^{-1}), and a tentative phase (0.05 cm yr^{-1}; dMAR = 400 g m^{-2} yr^{-1}) at 2700−3000 a (Fig. 14). Globally, these rates of sedimentation are an order of magnitude higher than those seen in typical mid-latitude loess sequences in China (Stevens and Lu, 2009) and Europe (Újvári et al., 2010), although episodes of extremely high sedimentation rate may also occur in some of these deposits too (Stevens et al., 2020). The rates observed in Adventdalen also greatly exceed loess accumulation rates in western Greenland (Willemse et al., 2003), central Sweden (Stevens et al., 2022), and Siberia (Volvakh et al., 2022), and exceed even the highest rates of loess accumulation observed in Alaska (Muhs et al., 2003). Indeed, only a single volcaniclastic-derived loess record in southern Iceland shows comparable rates of mid-late Holocene loess accumulation (Jackson et al., 2005). Even with relatively low estimated dry bulk density and relatively high organic matter content, these sedimentation rates translate into globally very high dMAR values of up to 2900 g m^{-2} yr^{-1} (Fig. 14). Typical dMAR values of well-dated (luminescence) loess sequences in Serbia do not exceed 350 g m^{-2} yr^{-1} (Perić et al., 2022), or 650 g m^{-2} yr^{-1} in Hungary, even with a highly resolved ^{14}C-based chronology (Újvári et al., 2017). On the Chinese Loess Plateau, last glacial dMAR rates derived from detailed independent dating are also lower than c. 300 g m^{-2} yr^{-1} (Stevens et al., 2016).

While such short-term, high rates of loess accumulation are only resolvable with extremely detailed independent dating, this trend to unusually high dust accumulation rates at CS-1 suggests that conditions in Adventdalen may be especially conducive to production and transport of wind-blown silts, making the area an unusually active, albeit local, dust source globally. If this is replicated over other similar valleys on Svalbard, it may suggest that the archipelago has been underappreciated as an active high-latitude dust source over the late Holocene generally. Indeed, although relatively few, modern observations point to recent dust activity in multiple areas of Svalbard (Di Mauro et al., 2022; Meinander et al., 2022). Testing this requires further detailed dating and analysis of loess records elsewhere in Adventdalen and Svalbard. Interestingly, observation of modern fine aeolian sandy sedimentation in

Ebbadalen in central Svalbard (Rymer et al., 2022) reveals sedimentation rates between 2012 and 2018 that are very similar to maximum rates observed in the CS-1 record. Luminescence and radiocarbon dating of a c. 900 yr long fine aeolian sand profile in the same study also suggests sedimentation rates at the low end of those observed in CS-1 (0.05 cm yr^{-1}).

We now discuss whether the changes in sedimentation rate observed at CS-1 can be linked to climatic drivers. We consider two main possibilities to explain the trends: wind activity and temperature control. Precipitation/humidity may also have a role to play, but is difficult to test from existing data and its influence on sedimentation rate is tied also to temperature. However, given that the source of the Adventdalen loess is the river floodplain, and given the low overall precipitation levels at the site, we consider that changes in precipitation are likely only to exert a secondary effect on sedimentation rate.

The peak in loess accumulation at 750−900 a coincides with two brief warming episodes in summer temperatures seen in a lake record in west Svalbard (D'Andrea et al., 2012), and broadly corresponds to Medieval Climate Anomaly (MCA) relative warmth seen in sea surface temperatures (Spielhagen et al., 2011; Werner et al., 2016) and reduced sea ice cover (Müller et al., 2012) in the eastern Fram Straight, as well as changes to warmer-demanding marine mollusc species around Svalbard (Mangerud and Svendsen, 2018). However, leaf wax hydrogen isotopic data from Hakluytvatnet lake in northwestern Svalbard suggest generally cooler conditions and polar air mass dominance over the entire period from 1800 to 180 a (Balascio et al., 2018), and there is no obvious change in sedimentation rate of sandy aeolian sediments in Ebbadalen in central Svalbard over this interval (Rymer et al., 2022). We note, however, that these sedimentation rates from Ebbadalen are derived from five ages over the 60 cm, 900 yr long sequence, and greater sampling resolution (as with CS-1 here) would be required to reveal short term changes in sedimentation rate.

Earlier peak phases of loess accumulation at c. 1050−1200, 1400−1600, 1900−2450 and 2700−3000 a (Fig. 14) also tentatively correlate to warm periods on Svalbard, while the most recent increase in dust accumulation (from c. 250 a) corresponds broadly to more recent warming observed in a number of records (D'Andrea et al., 2012). Increased sea surface temperatures in the Fram Strait (Spielhagen et al., 2011) and summer temperature increases in west Svalbard (D'Andrea et al., 2012) occur around 1100−1200 a, while a warmer phase between two glacial advances was identified between c. 1000 and 1200 a in southern Svalbard (Baranowski and Karlén, 1976), with possible reduced sea ice extent in the Fram Strait over the same interval (Müller et al., 2012). At 1500 a, sea surface temperatures also increased in the Fram Strait (Spielhagen et al., 2011), and reconstructed summer air temperatures remained high between 1400 and 1600 a in west Svalbard (D'Andrea et al., 2012). However, reconstructed sea ice extents in the Fram Strait (Müller et al., 2012) and temperatures in NW Svalbard (Balascio et al., 2018) are variable over this interval. Temperature reconstructions become much rarer prior to 2000 a, but the Hakluytvatnet record of NW Svalbard suggests higher temperatures and less polar air mass influence at c. 2000 a (Balascio et al., 2018), matching the significantly enhanced loess accumulation at 1900−2450 a, while Svendsen and Mangerud (1997) identify a warming phase on Svalbard around 2500−3000 a, corresponding to the earliest loess sedimentation peak at CS-1 (Fig. 14). This latter phase may also correspond to warmth in the Hakluytvatnet record (Balascio et al., 2018), although the resolution of this record is greatly reduced prior to 2000 a. By contrast though, a driftwood minimum on Svalbard over this period could be interpreted to imply persistent land-fast ice (Farnsworth et al., 2020).

Chronologies of glacial advances offer an even more confusing picture, with, for example, evidence for advances in central Svalbard at 1400−1600 a (Werner, 1993) and 1600−1800 a (Røthe et al., 2015), although it is clear that many glaciers show general advancing patterns over the whole last 4000 yrs (Farnsworth et al., 2020), coincident with Neoglacial cooling (Sejrup et al., 2016). However, the driver of glacial advances remains uncertain (Farnsworth et al., 2020), with the possible influence of low temperatures (Humlum et al., 2005), increased precipitation (Røthe et al., 2015), and lagged responses (time to reach equilibrium) to long term cooling initiated at 1800 a (Balascio et al., 2018), all being evoked.

As such, while there is a possible correlation between periods of loess sedimentation rate/dMAR increase and higher temperatures, we note that currently past temperature data from the region is sparse, and not always in agreement. Another possibility is that periodic heightened wind speeds or increased numbers of high wind speed events may also explain the increases in loess accumulation rate. Interestingly, the correspondence of increases in U ratio with sedimentation rate in the CS-1 record (Fig. 14) may support such a windiness driver for enhanced loess accumulation, as U ratio is often taken as an indicator of intensity of aeolian activity (Vandenberghe and Nugteren, 2001). In addition, increased snow drifting under windier periods could lead to more niveoaeolian sediment transport, further enhancing accumulation rates of loess. However, no independent evidence is available to test this hypothesis, and warmer climate phases may in any case coincide with periods of enhanced wind activity, and temperature-driven increases in both sediment load and fluvially transported sediment grain size may also be coincident in the river. Notably though, if temperature increases were the driver of the short-term loess accumulation rate peaks, this would contrast with the overall longer-term trend of increasing rate of loess sedimentation under a cooling Neoglacial climate observed at CS-1.

Any possible relationship between enhanced loess accumulation and warmer climate phases would appear to run contrary to the view that it is low humidity and high wind speeds that control cold climate aeolian activity (Sepällä, 2004; Jackson et al., 2005), and would seem at first to contradict experimental evidence that lower temperatures promote enhanced aeolian activity, due to greater air density (McKenna Neuman, 2004). However, modern observations of aeolian activity in Ebbadalen valley in central Svalbard also show a strong relationship between increased sediment accumulation and higher temperatures (Rymer et al., 2022). Higher recent sedimentation rates in Ebbadalen compared to LIA values also suggest higher temperatures drive enhanced aeolian activity in the valley over longer timescales. Furthermore, the importance of changes in source sediment supply has also been noted in modern observations (Bullard and Austin, 2011) and for Holocene loess deposits (Dijkmans and Tørnqvist, 1991; Willemse et al., 2003) in western Greenland, where increases in glaciofluvial activity are strongly associated with aeolian activity and loess deposition. Rymer et al. (2022) propose that supply and availability of source sediment for aeolian activity explain the correlation of warmer temperatures with increased aeolian depoition in Ebbadalen, and that changes in air density with temperature are not significant enough to affect aeolian transport. Such a temperature-driven sediment supply and availability mechanism for loess deposition may also operate in Adventdalen over the last 3000 yrs. Under this scenario, during warmer phases, enhanced melting of glaciers would have led to higher discharge rates and sediment loads in the Advent River, increasing sediment supply to the source of Adventdalen loess. During late summer and autumn when river levels drop (Fig. 3), larger volumes of this sediment

would have been exposed in the river floodplain, enhancing sediment availability for deflation and deposition as loess, and potentially leading to higher loess accumulation rates. Strong winds in autumn originating from the east (Fig. 2) would act as a transport agent for these silts. Decreased sediment availability during cold periods, and potentially increased vegetation cover leading to greater dust trapping during warm periods, may also play a role in modulating temperature control on dust accumulation as loess.

However, given the often inconsistent picture provided by independent records of temperature on Svalbard, the impact of sediment reworking on the upper part of CS-1, and the likely diversity of preserved loess records in Adventdalen, any effect of temperature or wind activity on loess accumulation requires further testing. Nonetheless, our results and the evidence for enhanced aeolian activity with temperature in Ebbadalen valley (Rymer et al., 2022) hints that a temperature-loess deposition coupling could be a wider trend, and that changes in aeolian activity and dustiness on Svalbard may be linked to temperature shifts. In any case, our results and those in Rymer et al. (2022) reveal very high rates of sediment accumulation relative to other high- and mid-latitude areas, at least locally where river beds act as sediment sources. This may imply that Svalbard is a far more important dust emitting region in the High Arctic than previously realised, potentially especially during warm climatic phases of glacier retreat. This suggestion would further imply that under modern and future climate warming there will be considerable increases in dust emission and deposition in Adventdalen, and possibly over Svalbard generally. Indeed, observations in Greenland point to intensification of dust events under recent warming (Saros et al., 2019) and periods of warmer than average conditions (van Soest et al., 2022), causing greater sediment supply to local outwash plain dust sources. Indeed several studies have argued that warming will increase dust emission in the high latitudes generally (Bullard et al., 2016; Meinander et al., 2022), with knock-on feedback effects. The record at CS-1 also shows somewhat increasing rates of loess deposition in the last few hundred yrs at the site (Fig. 14). Given that the current rate of warming on Svalbard far exceeds the global average (Nordli et al., 2020), this may suggest a highly active and dynamic interaction of climate and dust on the archipelago, which potentially impacts Arctic amplification, and could lead to significantly enhanced dust activity and emission from a warmer Svalbard in the future.

6. Conclusions

Extremely high sampling resolution quartz SAR OSL dating of a loess sediment core in Adventdalen, Svalbard reveals substantial changes in loess sedimentation rate over the last 3000 yrs. In general, the 136 quartz luminescence ages taken at 2 cm intervals are fast component dominated, pass internal SAR tests, and show good stratigraphic agreement. A Bayesian age model developed based on these ages allows resolution of sedimentation rate peaks with uncertainty ranging from $<\pm50$ to ±100 yrs at 1σ. This represents the most detailed luminescence dating undertaken to date on a sedimentary archive. Loess deposition was generally continuous over the last 3000 yrs, but during the Little Ice Age niveo-fluvial reworking or other sub-aqueous deposition briefly occurred at the site. Permafrost development was mostly syngenetic during loess formation, with decreasing ice contents upwards away from underlying peat and fluvial sediments. This decreasing ice content up section broadly coincides with increasing loess sedimentation rates through time and local lifting of the terrain surface due to this sedimentation.

Reconstructed loess sedimentation rate and dust mass accumulation rate (dMAR) peaks occur during the last 250 yrs, as well as

at 750−900, 1050−1200, 1400−1600, 1900−2450, and possibly 2700−3000 a. Higher relative coarse silt abundances, as expressed in the U-ratio, generally coincide with these higher sedimentation rate intervals. This coincidence potentially suggests greater wind activity drives the periods of enhanced dust activity and loess deposition. However, the individual sedimentation rate and dMAR peaks also seem to broadly coincide with possible warm phases on Svalbard, which may suggest a link with temperature-driven sediment availability in glaciofluvial source areas. Under this scenario, higher temperatures would drive enhanced glacier melting, higher stream flow in the Advent River, and enhanced sediment loads. This extra sediment would partially be deposited on the river floodplain and then be available for deflation and deposition as loess. However, both possible scenarios for enhanced loess accumulation are not mutually exclusive and require further testing, while the precise nature and extent of the sub-aqueous sedimentation or reworking during the Little Ice Age also remains to be constrained.

Overall, the derived rates of loess deposition in the Adventdalen core (sedimentation rates up to 0.35 cm yr^{-1} and dMAR values up to 2900 g m^{-2} yr^{-1}) are unusually high seen in a global perspective, and exceed those derived for other loess deposits in the mid and high latitudes. If representative of wider patterns across Svalbard in similar geomorphic valley settings, this may suggest the archipelago is a more important high latitude dust source than previously realised. Furthermore, if enhanced dust deposition is indeed driven by warming, this implies future climate warming would enhance dust generation in Svalbard even further.

Author statement

CFR, HHC, JPB and MFK designed the study. CFR, JPB, TS and RS undertook fieldwork. CFR and JPB conducted luminescence dating analyses, and JPB and AC undertook dose rate analyses and age modelling. CFR, RS and TS conducted grain size analyses and CFR and HHC undertook cryostratigraphic analyses. TS and CFR interpreted the data with input from all authors. TS and CFR wrote the manuscript, while all authors contributed to its revision and the final version.

Declaration of competing interest

The authors declare that they have no known competing financial interests or personal relationships that could have appeared to influence the work reported in this paper.

Data availability

Data is available in supplementary files.

Acknowledgements

Appendix A. Supplementary data

Supplementary data related to this article can be found at https://doi.org/10.1016/j.quascirev.2023.108137.

References

Adebiyi, A.A., Kok, J.F., 2020. Climate models miss most of the coarse dust in the atmosphere. Sci. Adv. 6 eaaz9507.

Albani, S., Mahowald, N.M., Winckler, G., Anderson, R.F., Bradtmiller, L.I., Delmonte, B., François, R., Gomanm, M., Heavens, N.G., Hesse, P.P., Hovan, S.A., Johfeld, K.E., Lu, H., Maggi, V., Mason, J.A., Mayewski, P.A., McGee, D., Miao, X., Otto-Bliesner, B.L., Perry, A.T., Pourmand, A., Roberts, H.M., Rosenbloom, N., Stevens, T., Sun, J., 2015. Twelve thousand years of dust: the Holocene global dust cycle constrained by natural archives. Clim. Past 11, 869–903.

Allen, J.R.L., 1962. Assymetrical ripple marks and the origin of cross-stratification. Nature 194, 167–169.

Autzen, M., Andersen, C.E., Bailey, M., Murray, A.S., 2022. Calibration quartz: an update on dose calculations for luminescence dating. Radiat. Meas. 157, 106828. https://doi.org/10.1016/j.radmeas.2022.106828.

Balascio, N.L., D'Andrea, W.J., Gjerde, M., Bakke, J., 2018. Hydroclimate variability of High Arctic Svalbard during the Holocene inferred from hydrogen isotopes of leaf waxes. Quat. Sci. Rev. 183, 177–187. https://doi.org/10.1016/j.quascirev.2016.11.036.

Baranowski, S., Karlén, W., 1976. Remnants of viking age Tundra in spitsbergen and northern scandinavia. Geogr. Ann. 58, 35–40.

Blaauw, M., Christen, J.A., 2011. Flexible paleoclimate age-depth models using an autoregressive gamma process. Bayesian Analysis 6, 457–474.

Bøtter-Jensen, L., Mejdahl, V., 1988. Assessment of beta dose-rate using a GM multicounter system. In: International Journal of Radiation Applications and Instrumentation. Part D. Nuclear Tracks and Radiation Measurements, vol. 14, pp. 187–191. https://doi.org/10.1016/1359-0189(88)90062-3.

Bryant, I.D., 1982. Loess deposits in lower adventdalen, spitsbergen. Polar Res. 1982, 93–103. https://doi.org/10.3402/polar.v1982i2.7006.

Bullard, J.E., Austin, M.J., 2011. Dust generation on a proglacial floodplain, West Greenland. Aeolian Research 3, 43–54. https://doi.org/10.1016/j.aeolia.2011.01.002.

Bullard, J.E., Baddock, M., Bradwell, T., Crusius, J., Darlington, E., Gaiero, D., Gassó, S., Gisladottir, G., Hodgkins, R., McCulloch, R., McKenna-Neuman, C., Mockford, T., Stewart, H., Thorsteinsson, T., 2016. High-latitude dust in the Earth system. Rev. Geophys. 54, 447–485. https://doi.org/10.1002/2016RG000518.

Cable, S., Elberling, B., Kroon, A., 2018. Holocene permafrost history and cry-ostratigraphy in the high-arctic Adventdalen valley, central svalbard. Boreas 47, 423–442. https://doi.org/10.1111/bor.12286.

Christiansen, H.H., Gilbert, G.L., Neumann, U., Demidov, N., Guglielmin, M., Isaksen, K., Osuch, M., Boike, J., 2021. Ground ice content, drilling methods and equipment and permafrost dynamics in Svalbard 2016-2019 (PermaSval). In: Moreno-Ibáñez, et al. (Eds.), SESS Report 2020, Svalbard Integrated Arctic Earth Observing System, Longyearbyen, pp. 259–275. https://doi.org/10.5281/zenodo.4294095.

Christiansen, H.H., Humlum, O., Eckerstorfer, M., 2013. Central svalbard 2000–2011 meteorological dynamics and periglacial landscape response. Arctic Antarct. Alpine Res. 45, 6–18. https://doi.org/10.1657/1938-4246-45.16.

Cresswell, A.J., Carter, J., Sanderson, D.C.W., 2018. Dose rate conversion parameters: assessment of nuclear data. Radiat. Meas. 120, 195–201. https://doi.org/10.1016/j.radmeas.2018.02.007.

Cunningham, A.C., Murray, A.S., Armitage, S.J., Autzen, M., 2018. High-precision natural dose rate estimates through beta counting. Radiat. Meas. 120, 209–214. https://doi.org/10.1016/j.radmeas.2018.04.008.

Cunningham, A.C., Buylaert, J.-P., Murray, A.S., 2022. Attenuation of beta radiation in granular sediment. Geochronology 4, 517–531. https://doi.org/10.5194/gchron-4-517-2022.

D'Andrea, W.J., Vaillencourt, D.A., Balascio, N.L., Werner, A.L., Roof, S.R., Retelle, M., Bradley, R.S., 2012. Mild Little Ice Age and unprecedented recent warmth in an 1800 year lake sediment record from Svalbard. Geology 40, 1007–1010. https://doi.org/10.1130/G33365.1.

Di Mauro, B., Cappelletti, D., Moroni, B., Mazzola, M., Gilardoni, S., Luks, B., Nawrot, A., Lewandowski, M., Dagsson Waldhauserova, P., Meinander, O., Wittmann, M., Kaspari, S., Kahn, A., 2022. Dust in Svalbard: local sources versus long-range transported dust (SVALDUST). In: Gevers, M., et al. (Eds.), SESS Report 2022, Svalbard Integrated Arctic Earth Observing System, Longyearbyen, pp. 62–77. https://doi.org/10.5281/zenodo.7377518.

Dijkmans, J.W.A., Tørnqvist, T.E., 1991. Modern periglacial eolian deposits and landforms in the Søndre Strømfjord area, West Greenland and their palae-oenvironmental implications. Meddelelser om Grønland. Geoscience 25, 1–39.

Eckerstorfer, M., Christiansen, H.H., 2011. The "high arctic maritime snow climate" in central svalbard. Arctic Antarct. Alpine Res. 43, 11–21. https://doi.org/10.1657/1938-4246-43.1.11.

Farnsworth, W.R., Allaart, L., Ingolfsson, O., Alexanderson, H., Forwick, M., Noormets, R., Retelle, M., Schomacker, A., 2020. Holocene glacial history of Svalbard: status, perspectives and challenges. Earth Sci. Rev. 208, 103249.

Fortier, D., Allard, M., Pivot, F., 2006. A late-Holocene record of loess deposition in ice-wedge polygons reflecting wind activity and ground moisture conditions, Bylot Island, eastern Canadian Arctic. Holocene 16, 635–646.

Førland, E.J., Benestad, R., Hanssen-Bauer, I., Haugen, J.E., Skaugen, T.E., 2011. Temperature and precipitation development at svalbard 1900–2100. Adv. Meteorol. 2011, 1–14. https://doi.org/10.1155/2011/893790.

French, H., Shur, Y., 2010. The principles of cryostratigraphy. Earth Sci. Rev. 101, 190–206. https://doi.org/10.1016/j.earscirev.2010.04.002.

French, H.M., Williams, P., 2017. The Periglacial Environment, fourth ed. Wiley Online Library.

Gilbert, G.L., Kanevskiy, M., Murton, J., 2016. Recent advances (2008-2015) in the study of ground ice and cryostratigraphy. Permafr. Periglac. Process. 27, 377–389.

Gilbert, G.L., O'Neill, H.B., Nemec, W., Thiel, C., Christiansen, H.H., Buylaert, J.-P., 2018. Late Quaternary sedimentation and permafrost development in a Sval-bard fjord-valley, Norwegian high Arctic. Sedimentology 65, 2531–2558. https://doi.org/10.1111/sed.12476.

Grinsted, A., Moore, J.C., Pohjola, V., Martma, T., Isaksson, E., 2006. Svalbard summer melting, continentality, and sea ice extent from the Lomonosovfonna ice core. J. Geophys. Res. 111, D07110. https://doi.org/10.1029/2005JD006494.

Hansen, V., Murray, A., Buylaert, J.-P., Yeo, E.-Y., Thomsen, K., 2015. A new irradiated quartz for beta source calibration. Radiat. Meas. 81, 123–127. https://doi.org/10.1016/j.radmeas.2015.02.017.

Humlum, O., Instanes, A., Sollid, J.L., 2003. Permafrost in Svalbard: a review of research history, climatic background and engineering challenges. Polar Res. 22, 191–215. https://doi.org/10.3402/polar.v22i2.6455.

Humlum, O., Elberling, B., Hormes, A., Fjordheim, K., Hansen, O.H., Heinermeier, J., 2005. Late-Holocene glacier growth in Svalbard, documented by subglacial relict vegetation and living soil microbes. Holocene 15, 396–407. https://doi.org/10.1191/0959683605hl817rp.

Jackson, M.G., Oskarsson, N., Trønnes, R.G., McManus, J.F., Oppo, D.W., Grönvold, K., Hart, S.R., Sachs, J.P., 2005. Holocene loess deposition in Iceland: evidence for millennial-scale atmosphere-ocean coupling in the North Atlantic. Geology 33, 509–512. https://doi.org/10.1130/G21489.1.

Jeppesen, J.W., 2001. Palæoklimatiske Indicatorer for Central Spitsbergen, Svalbard. Eksemplifi Ceret Ved Studier Af Iskiler Og Deres Værtssedimenter. Unpublished MSc Thesis. The University Centre in Svalbard.

Kohfeld, K., Harrison, S.P., 2003. Glacial-interglacial changes in dust deposition on the Chinese Loess Plateau. Quat. Sci. Rev. 22, 1859–1878.

Kottek, M., Grieser, J., Beck, C., Rudolf, B., Rubel, F., 2006. World Map of the Köppen-Geiger climate classification updated. Meteorol. Z. 15, 259–263. https://doi.org/10.1127/0941-2948/2006/0130.

Major, H., Nagy, J., 1972. Geology of the Adventdalen Map Area with a Geological Map, Svalbard C9G 1: 100 000. Norsk Polarinstitutt Skrifter Nr. 138 Norsk Polar Institutt Oslo 1972.

Mangerud, J., Svendsen, J.I., 2018. The Holocene thermal maximum around svalbard, arctic north atlantic; molluscs show early and exceptional warmth. Holocene 28, 65–83. https://doi.org/10.1177/0959683617715701.

McKenna Neuman, C., 2004. Effects of temperature and humidity upon the trans-port of sedimentary particles by wind. Sedimentology 51, 1–17.

Medialdea, A., Thomsen, K.J., Murray, A.S., Benito, G., 2014. Reliability of equivalent-dose determination and age-models in the OSL dating of historical and modern palaeoflood sediments. Quat. Geochronol. 22, 11–24.

Meinander, O., Dagsson-Waldhauserova, P., Amosov, P., Aseyeva, E., Atkins, C., Baklanov, A., Baldo, C., Barr, S.L., Barzycka, B., Benning, L.G., Cvetkovic, B., Enchili, P., Frolov, D., Gassó, S., Kandler, K., Kasimov, N., Kavan, J., King, J., Koroleva, T., Krupskaya, V., Kulmala, M., Kusiak, M., Lappalainen, H.K., Laska, M., Lasne, J., Lewandowski, M., Luks, B., McQuaid, J.B., Moroni, B., Murray, B., Möhler, O., Nawrot, A., Nickovic, S., O'Neill, N.T., Pejanovic, G., Popovicheva, O., Ranjbar, K., Romanias, M., Samonova, O., Sanchez-Marroquin, A., Schepanski, K., Semenkov, I., Sharapova, A., Shevnina, E., Shi, Z., Sofiev, M., Thevenet, F., Thorsteinsson, T., Timofeev, M., Silas Umo, N., Uppstu, A., Urupina, D., Varga, G., Werner, T., Arnalds, O., Vukovic Vimic, A., 2022. Newly identified climatically and environmentally significant high-latitude dust sources. Atmos. Chem. Phys. 22, 11889–11930.

Müller, J., Werner, K., Stein, R., Fahl, K., Moros, M., Jansen, E., 2012. Holocene cooling culminates in sea ice oscillations in Fram Strait. Quat. Sci. Rev. 47, 1–14. https://doi.org/10.1016/j.quascirev.2012.04.024.

Muhs, D.R., Ager, T.A., Bettis III, E.A., McGeehin, J., Been, J.M., Begét, J.E., Pavich, M.J., Stafford Jr., T.W., Stevens, D.A.S.P., 2003. Stratigraphy and palaeoclimatic sig-nificance of Late Quaternary loess–palaeosol sequences of the Last Interglacial–Glacial cycle in central Alaska. Quat. Sci. Rev. 22, 1947–1986.

Murray, A.S., Wintle, A.G., 2000. Luminescence dating of quartz using an improved single-aliquot regenerative-dose protocol. Radiat. Meas. 32, 57–73. https://doi.org/10.1016/S1350-4487(99)00253-X.

Murray, A.S., Wintle, A.G., 2003. The single aliquot regenerative dose protocol: potential for improvements in reliability. Radiat. Meas. 37, 377–381.

Murray, A.S., Marten, R., Johnston, A., Martin, P., 1987. Analysis for naturally occurring radionuclides at environmental concentrations by gamma spec-trometry. Journal of Radioanalytical and Nuclear Chemistry Articles 115, 263–288. https://doi.org/10.1007/BF02037443.

Murray, A.S., Helsted, L.M., Autzen, M., Jain, M., Buylaert, J.P., 2018. Measurement of natural radioactivity: calibration and performance of a high-resolution gamma spectrometry facility. Radiat. Meas. 15, 215–220.

Nordli, Ø., Wyszyński, P., Gjelten, H.M., Isaksen, K., Łupikaza, E., Niedźwiedź, T.,

Przybylak, R., 2020. Revisiting the extended Svalbard Airport monthly temperature series, and the compiled corresponding daily series 1898–2018. Polar Res. 39, 1–15.

Oliva, M., Vieira, G., Pina, P., Pereira, P., Neves, M., Freitas, M.C., 2014. Sedimentological characteristics of ice-wedge polygon terrain in Adventdalen (Svalbard) – environmental and climatic implications for the late Holocene. Solid Earth 5, 901–914. https://doi.org/10.5194/se-5-901-2014.

Overland, J., Dunlea, E., Box, J.E., Corell, R., Forsius, M., Kattsov, V., Skovgård Olsen, M., Pawlak, J., Reiersen, L.-O., Wang, M., 2019. The urgency of Arctic change. Polar Science 21, 6–13.

Perić, Z., Lagerbäck, E.A., Stevens, T., Ujvari, G., Zeeden, C., Buylaert, J.-P., Marković, S.B., Hambach, U., Fischer, P., Schmidt, C., Schulte, P., Lu, H., Yi, S., Lehmkuhl, F., Obreht, I., Veres, D., Thiel, C., Frechen, M., Jain, M., Vött, A., Zöller, L., Gavrilov, M.J., 2019. Quartz OSL dating of late quaternary Chinese and Serbian loess: a cross Eurasian comparison of dust mass accumulation rates. Quat. Int. 502, 30–44.

Perić, Z.M., Stevens, T., Obreht, I., Hambach, U., Lehmkuhl, F., Marković, S.B., 2022. Detailed luminescence dating of dust mass accumulation rates over the last two glacial-interglacial cycles from the Irig loess-palaeosol sequence, Carpathian Basin. Global Planet. Change 215, 103895.

Prescott, J.R., Hutton, J.T., 1994. Cosmic ray contributions to dose rates for luminescence and ESR dating: large depths and long-term time variations. Radiat. Meas. 23, 497–500.

Rymer, K.G., Rachlewicz, G., Buchwal, A., Temme, A.J.A.M., Reimann, T., van der Meij, W.M., 2022. Contemporary and past aeolian deposition rates in periglacial conditions (Ebba Valley, central Spitsbergen). Catena 211, 105974.

Roberts, H.M., 2008. The development and application of luminescence dating to loess deposits: a perspective on the past, present and future. Boreas 37, 483–507.

Roberts, H.M., Wintle, A.G., 2001. Equivalent dose determinations for polymineralic fine-grains using the SAR protocol: application to a Holocene sequence of the Chinese Loess Plateau. Quat. Sci. Rev. 20, 859–863.

Røthe, T.O., Bakke, J., Vasskog, K., Gjerde, M., D'Andrea, W.J., Bradley, R.S., 2015. Arctic Holocene glacier fluctuations reconstructed from lake sediments at Mitrahalvøya, Spitsbergen. Quat. Sci. Rev. 109, 111–125. https://doi.org/10.1016/j.quascirev.2014.11.017.

Saros, J.E., Anderson, N.J., Juggins, S., McGowan, S., Yde, J.C., Telling, J., Bullard, J.E., Yallop, M.L., Heathcote, A.J., Burpee, B.T., Fowler, R.A., Barry, C.D., Northington, R.M., Osburn, C.L., Pla-Rabes, S., Mernild, S.H., Whiteford, E.J., Andrews, M.G., Kerby, J.T., Post, E., 2019. Arctic climate shifts drive rapid ecosystem responses across the West Greenland landscape. Environ. Res. Lett. 14, 074027.

Schaetzl, R.J., Attig, J.W., 2013. The loess cover of northeastern Wisconsin. Quat. Res. 79, 199–214.

Schaetzl, R.J., Bettis, E.A., Crouvi, O., Fitzsimmons, K.E., Grimley, D.A., Hambach, U., Lehmkuhl, F., Markovic, S.B., Mason, J.A., Owraek, P., Roberts, H.M., Rousseau, D.-D., Stevens, T., Vandenberghe, J., Zarete, M., Veres, D., Yang, S., Zech, M., Conroy, J.L., Dave, A.K., Faust, D., Hao, Q., Obreht, I., Prud'homme, C., Smalley, I., Tripaldi, A., Zeeden, C., Zech, R., 2018. Approaches and challenges to the study of loess – introduction to the LoessFest special issue. Quat. Res. 89, 563–618.

Sejrup, H.P., Seppä, H., McKay, N.P., Kaufman, D.-S., Geirsdottir, A., de Vernal, A., Renssen, H., Husum, K., Jennings, A., Andrews, J.T., 2016. North Atlantic-Fennoscandian Holocene climate trends and mechanisms. Quat. Sci. Rev. 147, 365–378.

Sepällä, M., 2004. Wind as a Geomorphic Agent in Cold Climates. Cambridge University Press.

Spielhagen, R.F., Werner, K., Sørensen, S.A., Zamelczyk, K., Kandiano, E., Budeus, G., Husum, K., Marchitto, T.M., Hald, M., 2011. Enhanced modern heat transfer to the arctic by warm atlantic water. Science 331, 450–453.

Stevens, T., Lu, H., 2009. Optically stimulated luminescence dating as a tool for calculating sedimentation rates in Chinese loess: comparisons with grain-size records. Sedimentology 56, 911–934. https://doi.org/10.1111/j.1365-3091.2008.01004.x.

Stevens, T., Buylaert, J.-P., Lu, H., Thiel, C., Murray, A., Frechen, M., Yi, S., Zeng, L., 2016. Mass accumulation rate and monsoon records from Xifeng, Chinese Loess Plateau, based on a luminescence age model. J. Quat. Sci. 31, 391–405.

Stevens, T., Sechi, D., Bradak, B., Orbe, R., Baykal, Y., Cossu, G., Tziavaras, C., Andreucci, S., Pascucci, V., 2020. Abrupt last glacial dust fall over Southeast England associated with the dynamics of the British-Irish Ice Sheet. Quat. Sci. Rev. 15, 106641.

Stevens, T., Sechi, D., Tsiavaras, C., Schneider, R., Banak, A., Andreucci, S., Hättestrand, M., Pascucci, V., 2022. Age, formation and significance of loess deposits in central Sweden. Earth Surf. Process. Landforms 47, 3276–3301.

Strand, S., Christiansen, H.H., Johansson, M., Åkerman, J., Humlum, O., 2020. Active layer thickening and controls on interannual variability in the Nordic Arctic. Permafr. Periglac. Process. 32, 47–58.

Svendsen, J.I., Mangerud, J., 1997. Holocene glacial and climatic variations on Spitsbergen, Svalbard. Holocene 7, 45–57. https://doi.org/10.1177/095968369700700105.

Tolgensbakk, J., Sørbel, L., Høgvard, K., 2000. Geomorphological and Quaternary Geological Map of Svalbard. Nr. 32. Temakart. Norsk Polarinstitutt.

Újvári, G., Kovács, J., Varga, G., Raucsik, B., Marković, S.B., 2010. Dust flux estimates for the Last Glacial Period in East Central Europe based on terrestrial records of loess deposits: a review. Quat. Sci. Rev. 29, 3157–3166.

Újvári, G., Kok, J.F., Varga, G., Kovács, J., 2016. The physics of wind-blown loess: implications for grain size proxy interpretations in Quaternary palaeoclimate studies. Earth Sci. Rev. 154, 247–278.

Újvári, G., Stevens, T., Molnár, M., Kovács, J., 2017. Coupled European and Greenland last glacial dust activity driven by North Atlantic climate. Proc. Natl. Acad. Sci. USA 114, E10632-E10638.

van der Bilt, W.G.M., Bakke, J., Vasskog, K., D'Andrea, W.J., Bradley, R.S., Ólafsdóttir, S., 2015. Reconstruction of glacier variability from lake sediments reveals dynamic Holocene climate in Svalbard. Quat. Sci. Rev. 126, 201–218. https://doi.org/10.1016/j.quascirev.2015.09.003.

Vandenberghe, D., De Corte, F., Buylaert, J.-P., Kučera, J., Van den haute, P., 2008. On the internal radioactivity in quartz. Radiat. Meas. 43, 771–775.

Vandenberghe, J., Nugteren, G., 2001. Rapid climatic changes recorded in loess successions. Global Planet. Change 28, 1–9.

van Soest, M.A.J., Bullard, J.E., Prater, C., Baddock, M.C., Anderson, N.J., 2022. Annual and seasonal variability in high latitude dust deposition, West Greenland. Earth Surf. Process. Landforms 47, 2393–2409. https://doi.org/10.1002/esp.5384.

Vandenberghe, J., 2013. Grain size of fine-grained windblown sediment: a powerful proxy for process identification. Earth Sci. Rev. 121, 18–30.

Volvakh, N.E., Kurbanov, R., Zykina, V.S., Murray, A.S., Stevens, T., Költringer, C.A., Volvakh, A.O., Malikova, D.G., Taratuninag, N.A., Buylaert, J.-P., 2022. First high-resolution luminescence dating of loess in Western Siberia. Quat. Geochronol. 73, 101377.

Watanabe, T., Matsuoka, N., Christiansen, H.H., Cable, S., 2017. Soil physical and environmental conditions controlling patterned-ground variability at a continuous permafrost site, svalbard: patterned ground variability at a continuous permafrost site, svalbard. Permafr. Periglac. Process. 28, 433–445. https://doi.org/10.1002/ppp.1924.

Werner, A., 1993. Holocene moraine chronology, Spitsbergen, Svalbard: lichenometric evidence for multiple Neoglacial advances in the Arctic. Holocene 3, 128–137. https://doi.org/10.1177/095968369300300204.

Willemse, N.W., Kostar, E.A., Hoogakker, B., van Tatenhove, F.G.M., 2003. A continuous record of Holocene eolian activity in West Greenland. Quat. Res. 59, 322–334. https://doi.org/10.1016/S0033-5894(03)00037-1.

Zech, M., Zech, R., Zech, W., Glaser, B., Brodowski, S., Amelung, W., 2008. Characterisation and palaeoclimate of a loess-like permafrost palaeosol sequence in NE Siberia. Geoderma 143, 281–295.

Zhu, Y., Jia, X., Qiao, J., Shao, M., 2019. What is the mass of the loess in the Loess Plateau of China? Sci. Bull. 64, 534–539.